RESEARCH ARTICLE | JUNE 24 2025

On environment-related instrumental effects of ROMY (ROtational Motions in seismologY): A prototype, multi-component, heterolithic ring laser array

Andreas Brotzer ■ ⑩ ; Heiner Igel ⑩ ; Felix Bernauer ⑩ ; Joachim Wassermann ⑩ ; Jan Kodet ⑩ ; Karl Ulrich Schreiber ⑩ ; Jannik Zenner ⑩ ; Simon Stellmer ⑩



Rev. Sci. Instrum. 96, 064502 (2025) https://doi.org/10.1063/5.0242127





Articles You May Be Interested In

Long-term digital frequency-stabilized laser source for large-scale passive laser gyroscopes

Rev. Sci. Instrum. (January 2020)

Deep underground rotation measurements: GINGERino ring laser gyroscope in Gran Sasso

Rev. Sci. Instrum. (March 2017)

Invited Review Article: Large ring lasers for rotation sensing

Rev. Sci. Instrum. (April 2013)





On environment-related instrumental effects of ROMY (ROtational Motions in seismologY): A prototype, multi-component, heterolithic ring laser array

Cite as: Rev. Sci. Instrum. 96, 064502 (2025); doi: 10.1063/5.0242127

Submitted: 2 October 2024 • Accepted: 10 May 2025 •

Published Online: 24 June 2025







Andreas Brotzer, 1.a) D Heiner Igel, D Felix Bernauer, D Joachim Wassermann, D Jan Kodet, D





Karl Ulrich Schreiber. Dannik Zenner. Dand Simon Stellmer





AFFILIATIONS

- Department of Earth and Environmental Sciences, Ludwig-Maximilians-Universität München, Theresienstraße 41, 80333 München, Germany
- ²Research Unit Satellite Geodesy, Geodetic Observatory Wettzell, Technical University of Munich, Sackenrieder Straße 25, 93444 Bad Kötzting, Germany
- ³Physikalisches Institut, Rheinische Friedrich-Wilhelms-Universität Bonn, Wegelerstraße 10, 53115 Bonn, Germany
- a) Author to whom correspondence should be addressed: andreas.brotzer@lmu.de URL: https://www.geophysik.uni-muenchen.de/de/Members/brotzer

ABSTRACT

Large-scale ring laser gyroscopes (RLGs) are essential scientific instruments to study a variety of geophysical phenomena. The first and so far only large-scale RLG array ROMY (ROtational Motions in seismologY) comprises four triangular, heterolithic, active RLGs and can provide high-quality, three-component rotational ground motion observations. Compared to other RLGs, often being located in underground laboratories, ROMY is a near-surface installation that is more exposed to environmental influences. The prototype design of ROMY could serve as a blueprint for high-sensitivity, six degree-of-freedom stations for geoscientific rotation sensing. Understanding and quantifying instrumental effects caused by its environment is, therefore, essential to enhance the design toward a stable and continuous operation. Geometric deformation of a heterolithic optical ring resonator introduces undesired instrumental drifts that are challenging to mitigate. Applying a classic correction for backscatter-induced errors, we achieve a reduction in short-term Sagnac frequency fluctuations of several millihertz. A new sensor network inside ROMY monitors key environmental parameters such as barometric pressure and temperature. In order to quantify deformation of the resonator, we use camera-based beam tracking and free spectral range measurements. Based on these observations, we discuss the current operational stability of ROMY and recovery methods. We relate the observed instrumental drifts to dominant environmental drivers. Using a linear, multivariate modeling approach, we can identify dominant drivers and reduce long-term drifts of the Sagnac frequency. A quantification and better understanding of environment-induced instrumental effects allows to develop strategies for a further improvement in operational stability.

© 2025 Author(s). All article content, except where otherwise noted, is licensed under a Creative Commons Attribution (CC BY) license (https://creativecommons.org/licenses/by/4.0/). https://doi.org/10.1063/5.0242127

NOMENCLATURE

RLG Ring Laser Gyroscope **ROMY** ROtational Motions in seismologY

BC **Backscatter Correction FSR** Free Spectral Range MLTI MuLtimode TrIgger Optical Ring Resonator

Northern ring of ROMY RU Western ring of ROMY RV RW Eastern ring of ROMY RΖ Horizontal ring of ROMY

RANSAC RANdom SAmple Consensus algorithm

VLBI Very Long Baseline Interferometry

I. INTRODUCTION

Large-scale ring laser gyros (RLGs) with perimeters of several meters were initially introduced in the geosciences to enhance the observations of the Earth's spin and fluctuations therein. Terrestrial RLGs provide observations with short-term resolution and complement the long-term, stable, but elaborate measurements using VLBI (Very Long Baseline Interferometry).² These sensors have also become of interest for seismological observations for the detection of local rotational motions, such as those induced by seismic wave fields from earthquakes (e.g., Refs. 3-7). For rotation sensing, in particular toward portable sensors, other technologies, such as inertial rotation sensing (e.g., Refs. 8 and 9), fiber-optic sensors (e.g., Refs. 10 and 11), or cold atom gyrometers (e.g., Ref. 12) exist; however, only RLGs provide broadband high-sensitive rotation rate measurements at this point. The sensitivity of a RLG is determined by its geometrical size, as increasing the side length also increases the resolution. A non-monolithic, thus heterolithic, design cannot be avoided for large-scale realizations of RLGs, which introduces geometrical instabilities. A monolithic realization with thermally stable baseplate supporting the RLG structure was achieved for the single-component G-ring laser installed at the Geodetic Observatory Wettzell, Germany. 1,13 This design concept enabled the successful observation of polar motion¹⁴ and length-of-day variations.² In order to monitor the complete Earth rotation vector, an array of at least three RLGs is required. The first large-scale RLG array, named ROMY (ROtational Motions in seismologY), was realized at the Geophysical Observatory Fürstenfeldbruck, Germany, in 2016. 15,16 A set of four triangular RLGs are assembled in a downward pointing, heterolithic, tetrahedral structure with side lengths of up to 12 m. 16 ROMY was constructed to provide high-resolution observations of the rotational seismic wavefield for all three components (as compared to existing one-component sensors), in addition to the classic three translational components. Given the dimensions of the RLG array, it could only be realized based on a heterolithic design, mounting the optical ring resonators (ORR) onto a concrete monument inside a near-surface concrete structure. 16 The design of ROMY could generally become a blueprint for high-sensitive, six degree-of-freedom stations for geoscientific rotation sensing. For seismological applications, a continuous record, thus operation, has to be ensured for at least three RLGs of the array. Beyond seismology, harnessing the potential for improved geodetic observations with ROMY, such as monitoring of the complete Earth rotation vector, polar motion, or length-of-day variations, with a terrestrial sensor, requires not only the given sensitivity, but also a high mechanical stability of the RLGs. In order to become a blueprint, the design-related susceptibilities to environmental influences have to be monitored, understood, and eventually controlled or mitigated. Identifying key drivers requires multi-parameter observations of environmental phenomena. Stability is essential for continuous data acquisition, thus facilitating further geophysical studies. In order to eventually exploit ROMY's theoretical sensitivity of 10⁻¹³ rad s⁻¹, in particular at long integration times (>10⁵ s), all restrictions due to external and internal effects on the stability have to be understood and mitigated. We provide new data and insights into the characterization of the near-surface, heterolithic RLG array ROMY with regard to instrumental effects. This allows us to propose customized strategies to reduce such instrumental effects by actively

stabilizing each ORR and/or develop models for correction during post-processing to enhance the final data quality.

In order to illustrate the observed challenges related to operational stability of the RLGs, we will first introduce the basic background on Sagnac gyroscopes, indicate potential instrumental effects, and provide an overview of the specific, structural design of ROMY and its environment.

A. Sagnac interferometry and instrumental effects

RLGs can be operated as active or passive optical interferometers in a Sagnac configuration, while for active RLGs, the resonator is filled with a mix of helium–neon gas medium (e.g., Ref. 1). Passive RLGs are under development (e.g., Ref. 17); however, we focus on active designs given the relevance for ROMY. Large-scale RLGs with sufficient sensitivity and stability can provide access to Earth's spin and variations therein (e.g., Ref. 2), as well as local rotational ground motions, such as induced by passing seismic waves of earthquakes (e.g., Refs. 3–5).

The Sagnac beat frequency δf (hereafter referred to as Sagnac frequency) for an RLG is given by

$$\delta f = \frac{4 A}{\lambda P} \vec{n} \vec{\Omega}, \tag{1}$$

where P is the perimeter, A is the encircled area, \vec{n} is the areal normal vector, and λ is the optical wavelength (=632.8 nm for a helium–neon laser).

The rotation rate Ω is a superposition of the Earth's spin rate Ω_E and a local rotation rate Ω_L ,

$$\delta f = \frac{4 A}{\lambda P} (|\vec{\Omega}_E| + |\vec{\Omega}_L|) \sin(\varphi + \theta) \cos(\gamma) + f_{bs}, \qquad (2)$$

where φ is the local latitude, γ is an azimuth tilt, f_{bs} is the backscatter error, and θ is a local tilt in the N–S direction. In case of an equilateral triangular-shaped resonator, the scale factor S can be expressed using the side length L,

$$S = \frac{4 A}{\lambda P} = \frac{\sqrt{3} L}{3 \lambda}.$$
 (3)

The sensitivity of a RLG (also referred to as ring laser or merely ring) is controlled by the scale factor S [see Eq. (3)].

First, the scale factor is affected by the geometrical variations of the ORR altering the side length [see Eq. (3)]. Second, variations in the sensor orientation, relative to the local normal vector, also affect the detected signal [see Eq. (1)]. An orientation change in the east—west direction scales with the cosine and is, therefore, inferior compared to changes in the north—south direction. Both are to be reduced to avoid instrumental effects on the Sagnac frequency. The wavelength of the active helium—neon lasers (λ = 632.8 nm) is altered due to internal lasing dynamics (e.g., Refs. 1, 18, and 19). Hurst *et al.*¹⁸ investigated subtle instrumental effects on the scale factor for the ultra-stable monolithic, active G-ring laser. In particular, the internal effects discussed by Hurst *et al.*¹⁸ are certainly present in ROMY's RLGs, but are of minor importance in this study, since external forces on the resonator's geometry are dominant at this point.

A monolithic design, as realized for the square 4×4 m² Gring, ¹³ is not feasible for larger RLGs. Therefore, heterolithic RLGs' higher sensitivity comes at the cost of less mechanical rigidity and requires mitigation or correction strategies. ^{1,19,20} This is true for passive RLG designs (e.g., Ref. 17) as well as for active designs.

B. Structural and environmental aspects of ROMY

ROMY, as described in detail by Igel *et al.*, 16 is a multicomponent large-scale RLG array and intends to provide high-sensitivity observations of rotational ground motions for seismology and geodesy. 15,16 The sensor is located at the site of the Geophysical Observatory in Fürstenfeldbruck, Germany. The four individual, triangular-shaped RLGs form a downward pointing tetrahedron inside a fiberglass reinforced concrete structure [Fig. 1(c)].

This includes a slightly smaller (L = 11.2 m) horizontally oriented RLG (RZ) and three slanted RLGs (RU, RV, and RW; L = 12 m), as indicated by red lines in Fig. 1(c). Simultaneous recordings of at least three RLGs allow reconstructing all three components of rotational ground motion. 15,16 The subsurface structure built from glass-fiber reinforced concrete includes seven independent access shafts with nine chambers [numbered 01–09; Fig. 1(c)]. The horizontal RLG is at a depth of about 2.5 m, and the tetrahedral tip is at about 14 m below the surface. The diagonal tubes toward the tip of the tetrahedron run inside a concrete monument that is not included in the sketch of Fig. 1(c), but illustrated in Igel *et al.* 16

In each corner chamber, three stainless-steel corner boxes (green/yellow) are fixed to the concrete monument or slanted gabbro monuments holding the corner boxes of the slanted RLGs, as indicated in the model of Fig. 1(b). The stainless steel tubes are fixed to the concrete monument, as is the gain tube. The gain tube

contains a 5 mm wide and 20 mm long capillary, serving as a spatial mode filter, which is aligned with four micrometer screws. ¹⁶ The stainless-steel tubes are connected to the corner boxes (blue) via stainless-steel bellows for mechanical decoupling [orange; Figs. 1(a) and 1(b)]. The dielectric corner mirrors are placed inside the corner boxes, thus inside the ORR [Fig. 1(a)]. The entire corner box incorporates two degrees-of-freedom, in-plane and out-of-plane, to align the mirrors using micrometer screws and levers and establish a closed beam path. The beam combination is performed using a Koesters prism [as shown in Fig. 1(a)] or with a beam splitter and two deflection mirrors.

Every scientific sensor is influenced by ambient environmental influences, which have to be understood and quantified. Resulting instrumental perturbations must be mitigated by either shielding or applying appropriate corrections.

The effects of ambient temperature and barometric pressure on ORR have been observed and reported for other RLGs, particularly those of heterolithic design (e.g., Refs. 1, 21, and 22). In contrast to other RLGs, located underground in the Cashmere caves (e.g., Ref. 1), the underground Gran Sasso Laboratory (e.g., Refs. 22 and 23), or a confined chamber at the observatory Wettzell, ¹³ ROMY is located near the surface, ¹⁶ as indicated in Fig. 1(c). With regard to this special design, the susceptibilities to external influences have to be quantified for ROMY separately, to eventually serve as guidance for potentially similar near-surface installations in the future.

II. DATA ACQUISITION AND OBSERVATIONS

We describe the additionally installed and operated sensors to monitor environmental changes and the acquired dataset.

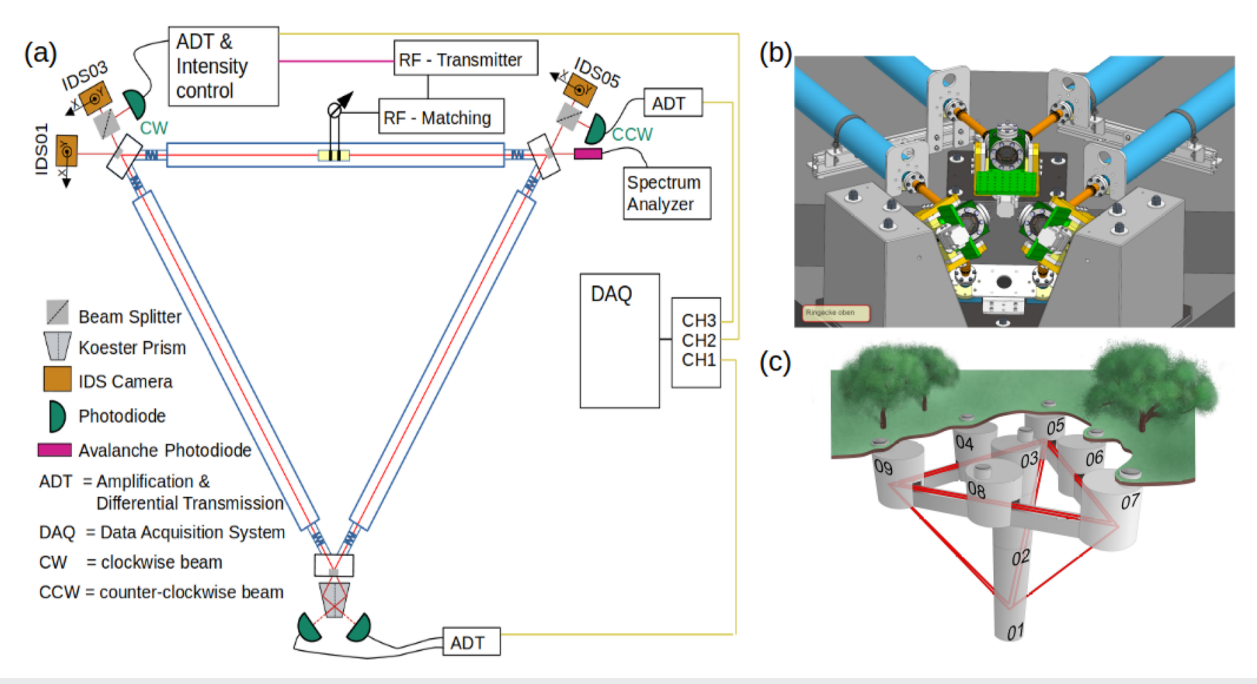


FIG. 1. (a) Schematic experimental setup for FSR measurement at RZ. (b) 3D model of an assembly of three corner boxes as found in shafts 05, 07, and 09. (c) Simplified near-surface ROMY structure with numbered access shafts. All sketches are not to scale.

Moreover, several exemplary observations of responses to external influences are presented.

A. Monitoring sensor network

In order to monitor environmental influences, a sensor network was installed inside ROMY's shafts in 2021. This network comprises a combined sensor for air temperature, air pressure, and air humidity inside each shaft [Fig. 1(c)]. A weather station (BW.FURT) at the surface next to ROMY provides observations for precipitation, surface air temperature, as well as barometric pressure and serves as an external reference. A light sensor automatically detects and logs maintenance activity inside the shafts. A two-component inertial tiltmeter (BW.ROMYT) is installed inside ROMY's southern shaft on the concrete monument, providing observations of local tilting of the monument. An infrasound sensor (BW.FFBI) inside shaft 03 provides infrasound and absolute air pressure observations. A groundwater gauge on the site of the Geophysical observatory (~200 m from ROMY) provides a reference for variations in nearsurface hydrology. A set of monochromatic video cameras by IDS imaging (see Table II) mounted behind the corner mirrors is used to monitor beam walk, which serves as a proxy for deformation at the corner.

A passive thermal insulation system was designed and implemented for access shafts 04–09 in 2024. This barrier acts successfully as a low-pass filter and suppresses previously present daily and sub-daily temperature perturbations. A decrease in thermal power level may be linked to reduced thermal convection inside the shafts with the thermal barrier. A seasonal trend, however, is no

mitigated and requires an active heating system in the future. A detailed description and discussion is provided in Appendix C.

B. Long-term Sagnac frequency drift

For an observational period between October 2023 and July 2024, three of ROMY's RLGs have been successfully operated together with the additional environmental sensor network. The computed Sagnac frequency is estimated based on a Hilbert demodulation approach¹⁶ and is shown in Fig. 2 from January to July 2024. The gaps represent intervals of non-operation or extended split-mode operation states. Non-operational intervals occur when a closed optical beam path inside the ORR is not given, for instance due to geometric misalignment of the ORR. This requires manual re-alignment efforts. Maintenance activity is indicated (yellow vertical bars) to explain artifacts related to the activity, such as frequency offsets due to a changed ORR geometry after re-alignment [see Fig. 2(a) around day 15 or Appendix F, Fig. 20]. Split-mode operation state occurs whenever the longitudinal mode index for the clockwise and counterclockwise propagating beams is different. Changing mode indices or activated higher resonator modes, maintaining the same index in both propagation directions, is referred to as mode jumps. The observed frequency drifts of the Sagnac beat frequency, as well as frequently occurring mode jumps and split-mode states, are mostly a result of geometric deformation of the ORR. A mechanically more rigid RLG, such as the monolithic G-ring, 13 is less susceptible to geometric deformation, thus resonator misalignment.

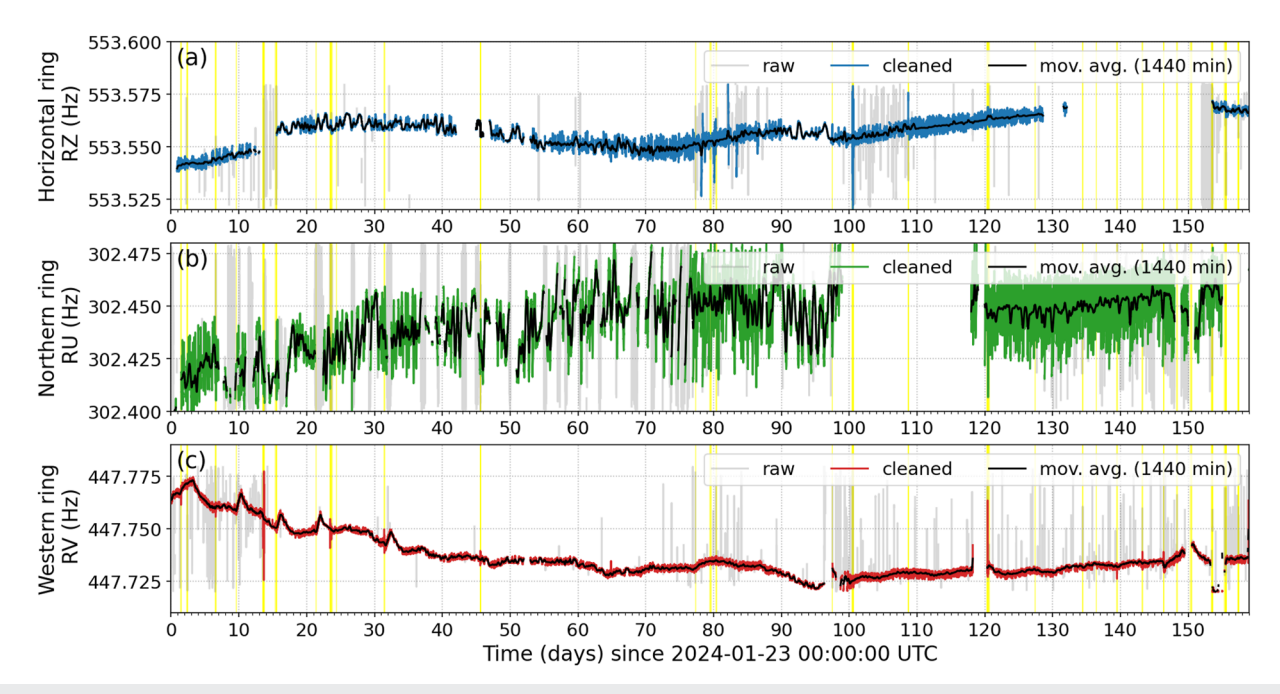


FIG. 2. Long-term drifts of Sagnac frequency over several months of ROMY's (a) horizontal ring RZ, (b) northern ring RU, and (c) western ring RV are shown. Colored traces are cleaned by removing times of logged MLTI launches (gray). The low-frequency drift is represented by applying a moving average (black) of 12 h (720 min). Yellow bars indicate time intervals of maintenance work.

All three RLGs reveal different long-term and short-term drift characteristics. A moving average is computed for 12 h windows to better capture the long-term drift. For this observational period, the maximum drift range for RZ, RU, and RV is about 30, 40, and 50 mHz, respectively. We attribute the significantly greater dynamics in short-term drifts, observed for RU, to a lower quality gas mix using natural neon gas (Ne²⁰), while RZ and RV are operated with an equal mix of Ne²⁰ and Ne²² isotopes to optimize the gain curve (see Ref. 1).

Geometric changes of the ORR affect the Sagnac frequency (see Sec. I A). Attributing a Sagnac frequency drift of 10 mHz to pure length change ΔL [Eq. (3)] would correspond to an elongation of about 202 μ m. An orientation change of the beam plane in the north-south direction θ [Eq. (3)] of 0.1 mrad would cause a frequency drift of 49.4 mHz.

For seismological observations, strong short-term drifts disrupt continuous observations due to split-mode operation states or misalignment, while mode jumps introduce discontinuities in rotation data. For geodetic signals such as polar motion or length-of-day variations, the observed long-term drifts are still orders of magnitude above the required stability of prad s⁻¹ at integration times of $10^5 - 10^6$ s (e.g., Refs. 1 and 2).

C. Geometric resonator deformation

1. Beam walk

In order to qualitatively capture the deformation of the ORR, we use a method that has been applied to other large heterolithic RLGs, such as UG-2. 1,24,25 The video camera is mounted behind the mirror, with the sensor perpendicular to a transmitted beam. Fitting a 2D-Gaussian distribution to the beam image of the camera allows inferring the beam maximum in the y-direction (out-of-plane) and x-direction (in-plane), resembling the degrees-of-freedom at the corner box [see Figs. 1(a) and 23]. The x-direction and y-direction of

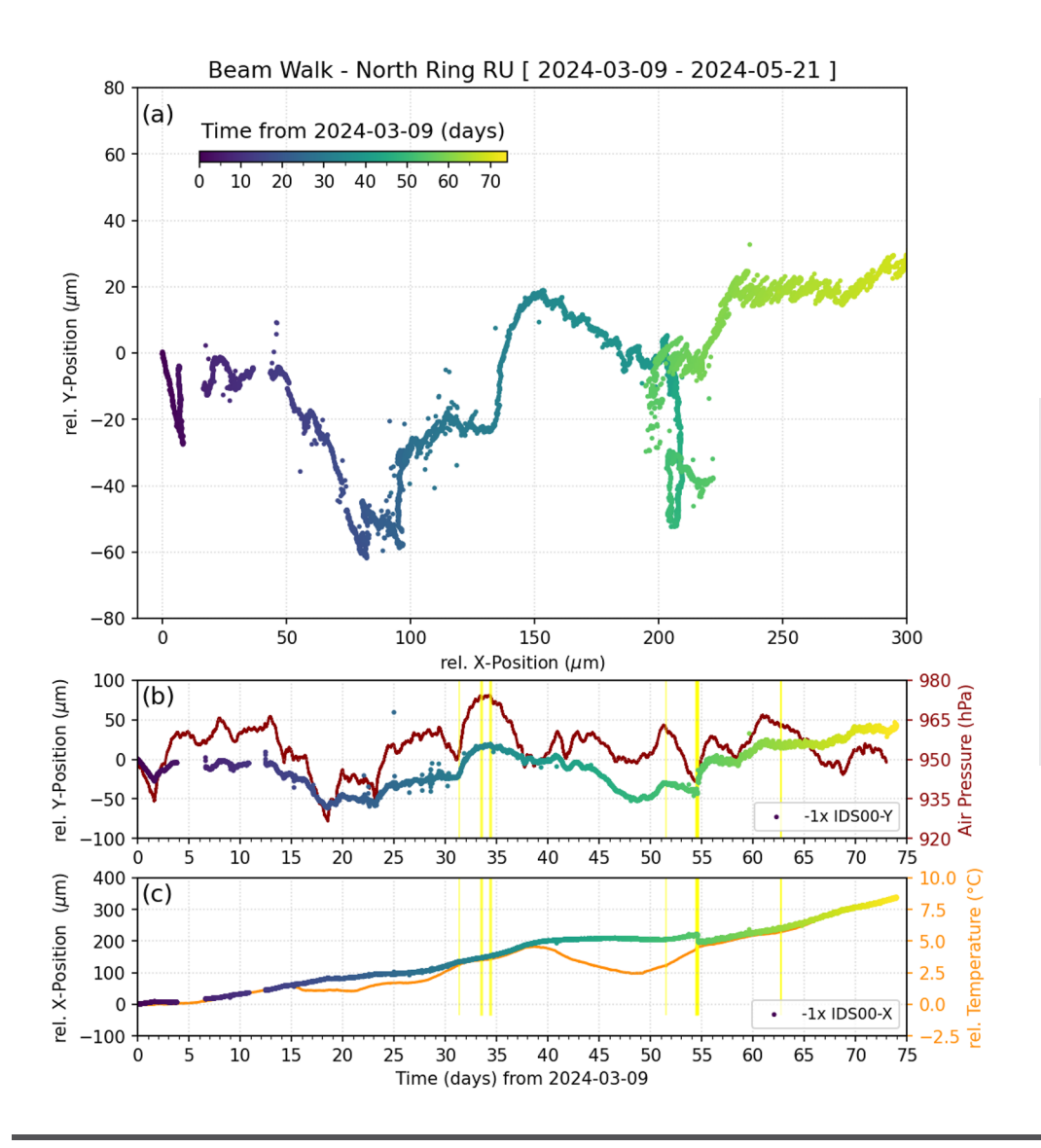


FIG. 3. (a) Beam peak position tracking as relative displacement in the x-direction (in-plane) and y-direction (out-of-plane) for the counter-clockwise monobeam of ROMY's northern ring RU at its northwestern corner over 74 days. (b) The out-of-plane displacement over time with barometric pressure. (c) The in-plane displacement and combined air temperature change at the resonator corners. The y- and x-displacements are reversed in all panels. The sampling rate for beam tracking is 10 min, and outliers are removed. The yellow vertical lines indicate maintenance periods.

the camera sensor [see Fig. 1(a)] can be converted to displacement (in micrometers) using the camera sensor's pixel size (see Table II). A triangular-shaped RLG is advantageous since the beam plane is well-defined at all times; however, it limits the amount of deployable cameras for beam tracking, while still recording Sagnac and monobeam signals.

Figure 3(a) shows the beam walk, based on the first deployed camera (IDS00) at the northwestern mirror of RU, over 74 days (March 09, 2024, to May 21, 2024) and reveals high dynamic in deformation. A relative beam displacement in the x-direction of about 340 μm is accumulated. This in-plane deformation is well correlated with the increasing summed air temperature at all corner shafts of the resonator [Fig. 3(b)]. The deformation in-plane seems to be dominantly controlled by thermal expansion, since at times of temperature decrease, the deformation is significantly reduced [Fig. 3(b)].

The relative beam displacement in the y-direction exposes more short-term dynamics covering a range of about -40 to 60 μ m. The variation appears to have some correlation with inverted changes in local barometric pressure [Fig. 3(c)]. For the heterolithic RLG UG-2 located in an underground cave with rather stable environmental conditions, Pritsch *et al.*²⁵ reported a maximal beam walk of about 30 μ m in the vertical direction and about 50 μ m in the horizontal direction over 2.5 days.

Note that the sudden offset on day 54 is attributed to minor resonator re-alignment during maintenance activity.

In order to monitor beam walk for both monobeams at one corner, two cameras (IDS01 and IDS03) were installed at the southern corner of RZ. The beam tracking over 23 days reveals a displacement in the y-direction of up to 80 μm with short-term variations and in the x-direction of up to 40 μm following a mostly linear trend [see Figs. 4(c) and 4(d)]. Both beam walk time series for the displacement in both directions correlate well. However, a diverging trend is evident for both monobeams, which amounts to 15 and 75 μm , for x- and y-positions, respectively, after 23 days.

We infer the beam intensity using the peak of the 2D-Gaussian fitted on the images. A relative beam intensity decrease of about 40% for IDS01 and only about 15% for IDS03 [Fig. 4(b)] is obtained. An intensity change might result from a change in the orthogonality of the transmitted beam onto the camera sensor due to beam walk. Small contributions to the observed divergence might result from slightly different distances of the camera sensor to the mirror, which is also the pivot point of the corner, thus amplifying displacements due to a different lever.

The peak-to-peak amplitude of the sinusoidal Sagnac interferogram shown in Fig. 4(a) reveals a decreasing trend, of about 0.7 V overall [Fig. 4(a)], and sudden offsets correlate well with the declining beam intensity. Thus, the change of the beam plane due

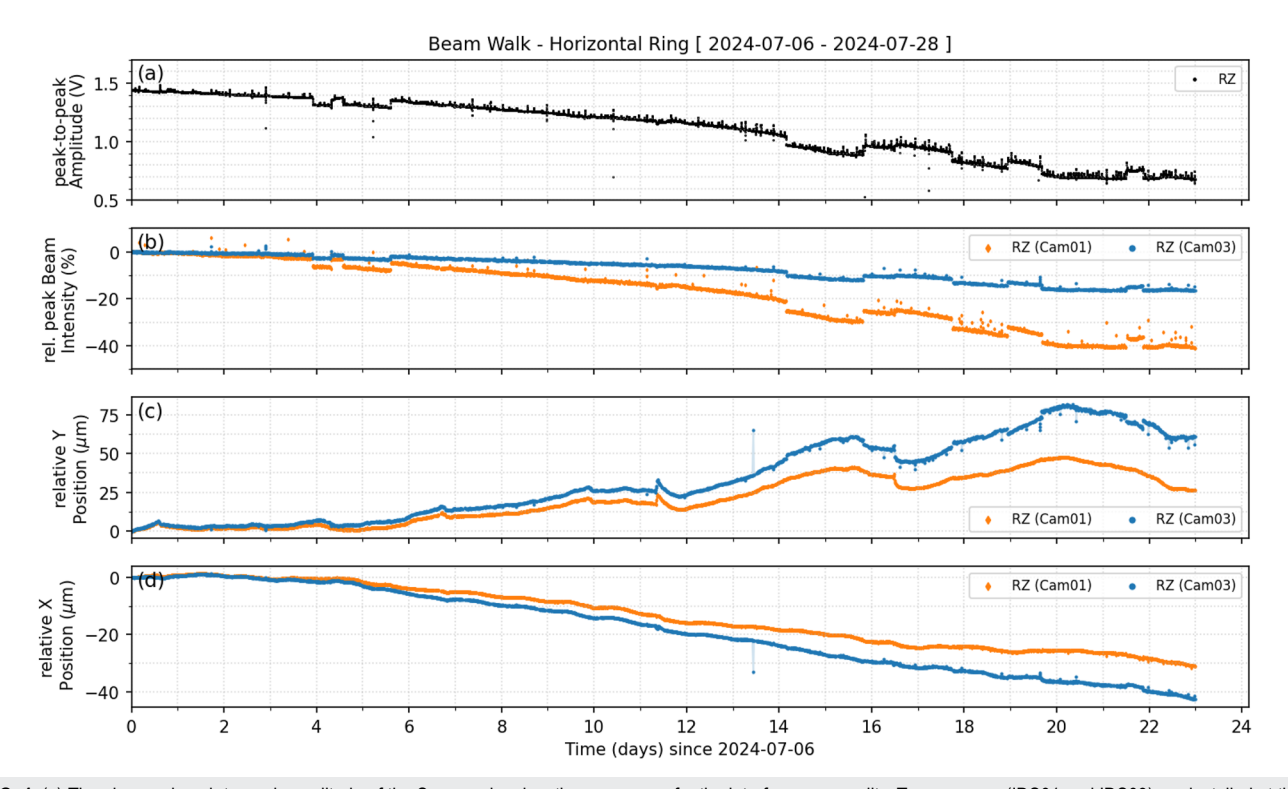


FIG. 4. (a) The observed peak-to-peak amplitude of the Sagnac signal, acting as a proxy for the interferogram quality. Two cameras (IDS01 and IDS03) are installed at the southern corner of the horizontal ring (RZ), observing (b) the relative maximal beam intensity (0–255) and the beam displacement (c) in the y-direction (=out-of-plane) and (d) in the x-direction (=in-plane) for both monobeams. The sampling rate is 10 min. Outliers have been removed.

to geometric resonator deformation clearly degrades the interferogram quality, eventually culminating in a resonator misalignment and complete fading of the interferogram. Several causes for reduced beam intensity are possible: (1) a decrease in overlapping area and alignment for the beam combination, (2) a reduction in the resonator finesse, thus beam intensity, by moving the reflection point on the mirrors, and (3) a shift in the beam plane causing misalignment with the constricted gain tube capillary.

This demonstrates the strong influence of deformation at the corners, resembled by beam walk, not only on the Sagnac signal quality but also on the scale factor and beam plane orientation.

2. Perimeter variation

Geometric deformation of the perimeter of the ORR affects the scale factor and can be measured by observing changes in the free spectral range (FSR),

$$n FSR = \frac{c}{P} , \qquad (4)$$

where c is the speed of light ($\approx 3 \times 10^8 \text{ m s}^{-1}$), n is the integer mode index, and P is the perimeter of the optical ring resonator (e.g., Ref. 1). For large RLGs, such as RZ with a perimeter of about 33.55 m, the FSR is small with 8.94 MHz. Considering a gain curve with a width of about 1.8 GHz, an operation on a stable phase-locked multimode regime is challenging to obtain. Monitoring the relative FSR variation over time using an adequate fast avalanche photodiode and a spectrum analyzer, stabilized with a 10 MHz GPS reference, enables tracking the changing perimeter [Eq. (4)]. A schematic setup of this experiment is illustrated in Fig. 1(a). Due to homogeneous

broadening inside the resonator, smaller longitudinal modes are suppressed. Of the excited FSR peaks, the 12th FSR peak (=107.2994 MHz) was found to be the most stable.

D. Thermal response

A response of the Sagnac frequency of RV to a temperature perturbation as a result of an extended interval of air ventilation is shown in Fig. 5. The sudden increase in temperature of up to 2.5 $^{\circ}$ C in the central shaft 01 is related to maintenance activity. The temperature at the other two corners of this resonator (07 and 09) is only slightly perturbed.

A pronounced response to the temperature perturbation, including a fast increase of about 6 mHz followed by a slower decay, is reflected as a variation of the Sagnac frequency of several megahertz. A thermal expansion of the ORR relates to an increase in scale factor, thus an increase in Sagnac frequency [see Eq. (3)]. The observed 6 mHz variation would correspond to a pure length change of about 160 μm , by assuming no change in the orientation of the beam plane in connection with thermal deformation at the corner(s). This is certainly a strong assumption. The slow temperature increase over 80 h of about 250 m $^{\circ}$ C is more pronounced for the upper shafts 07 and 09 and related to seasonal warming (not mitigated by the passive thermal insulation).

The drift signatures in the Sagnac frequency as a response to temperature changes are observed for all RLGs of ROMY, in particular for uncontrolled perturbations during and after maintenance activity. Several upward drifts due to the thermal expansion of the resonator followed by relaxing contraction are clearly visible for RV in Fig. 2(c).

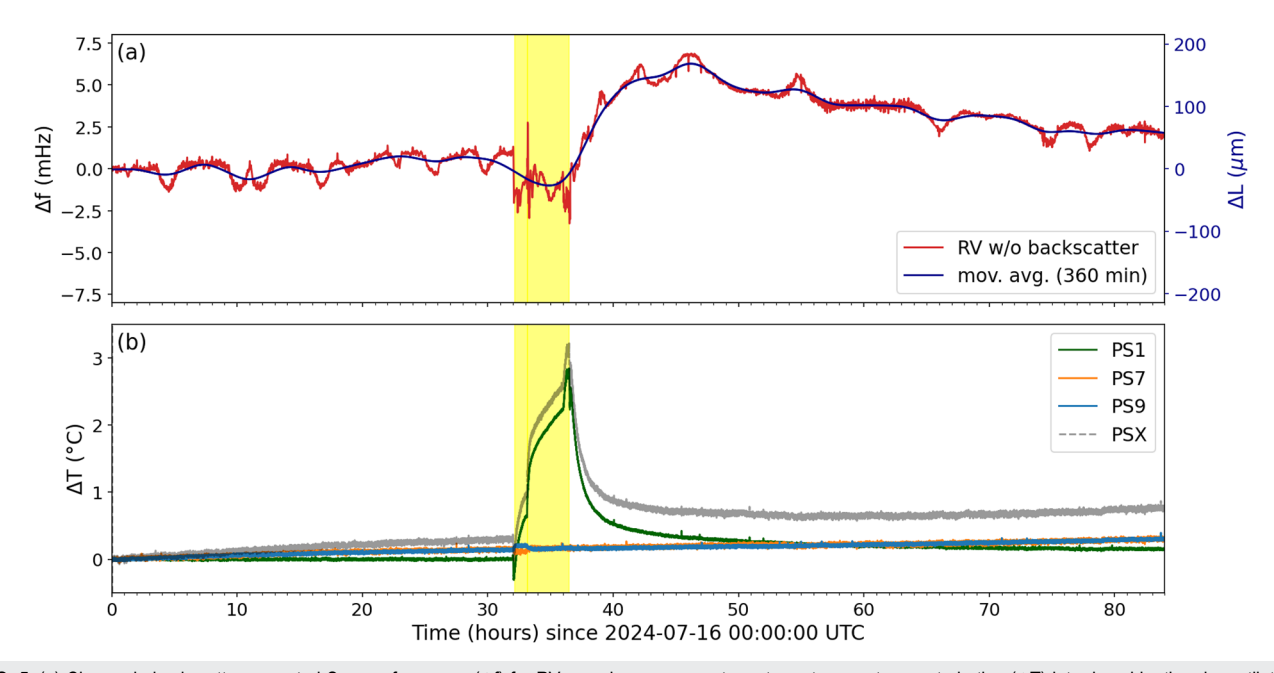


FIG. 5. (a) Change in backscatter-corrected Sagnac frequency (Δf) for RV reveals a response to a strong temperature perturbation (ΔT) introduced by the air ventilation system in the central shaft operated during maintenance activity (yellow patch). The right y-axis shows the corresponding resonator side length variation (ΔL). (b) The temperature change in central shaft (PS1) and corner shafts of RV (PS7 and PS9), while PSX represents a summed temperature variation across all three corners.

We relate temperature variations at the corners to integrated thermal strain along the resonator. A length change of one optical wavelength is expected to promote mode jumps. The inferred linear thermal expansion coefficients are comparable to common values for concrete ²⁶ or structural steel. ²⁷ Detailed information is provided in Appendix D.

E. Barometric response

An example of the barometric response at RZ to a passing low-pressure system around midday of May 06, 2024, introducing a barometric pressure drop of about 10 hPa is shown in Fig. 6. The low-frequent, backscatter-corrected Sagnac frequency of RV correlates well with the barometric pressure, and a relative change of approximately -1.6 mHz is observed [Fig. 6(c)].

For this event, the peak beam displacement in the reversed y-direction ($\approx\!-6~\mu m)$ is about ten times more pronounced compared to the x-direction ($\approx\!0.6~\mu m)$ for cameras at RZ. There is a clear correlation (CC = 0.8) between the local barometric pressure and the reversed y-direction of the beam displacement [Fig. 6(a)]. Observations of a co-located inertial Lippmann tiltmeter ROMYT confirm E–W tilt deformation at the corner basement exceeding the tidal deformation at the time during minimum air pressure. Tilt deformation in the N–S direction is less pronounced (Fig. 6).

The Hilbert transform of the barometric pressure can be used to approximate the surface deformation in the surrounding area by a traveling pressure wave. Here, no obvious correlation is found for the Hilbert transform; thus, most deformation is, instead, caused due to deformation of the monument inside access shafts, acting as subsurface cavities.

A second example for pressure loading induced deformation at the resonator corner is provided in Fig. 24, supporting the presented observations.

F. Hydrologic response

The near-surface, concrete ROMY structure is in the depth range of a near-surface groundwater layer. Variations of the groundwater table, in particular after heavy rain, are expected to exert asymmetric hydrostatic pressure on the ROMY structure as well as increasing loads inside the refilled volume of the ROMY structure. Both are expected to contribute to the deformation of the structure, especially due to orientation changes. Assuming that the entire ROMY structure behaves monolithically (hence, no internal deformation), the overall change in orientation should be resembled complementary on all four Sagnac frequencies. At the moment, this effect cannot be constrained with the available observations. We expect at this point that temperature (and pressure) influences dominate. By having all rings operating with backscatter correction

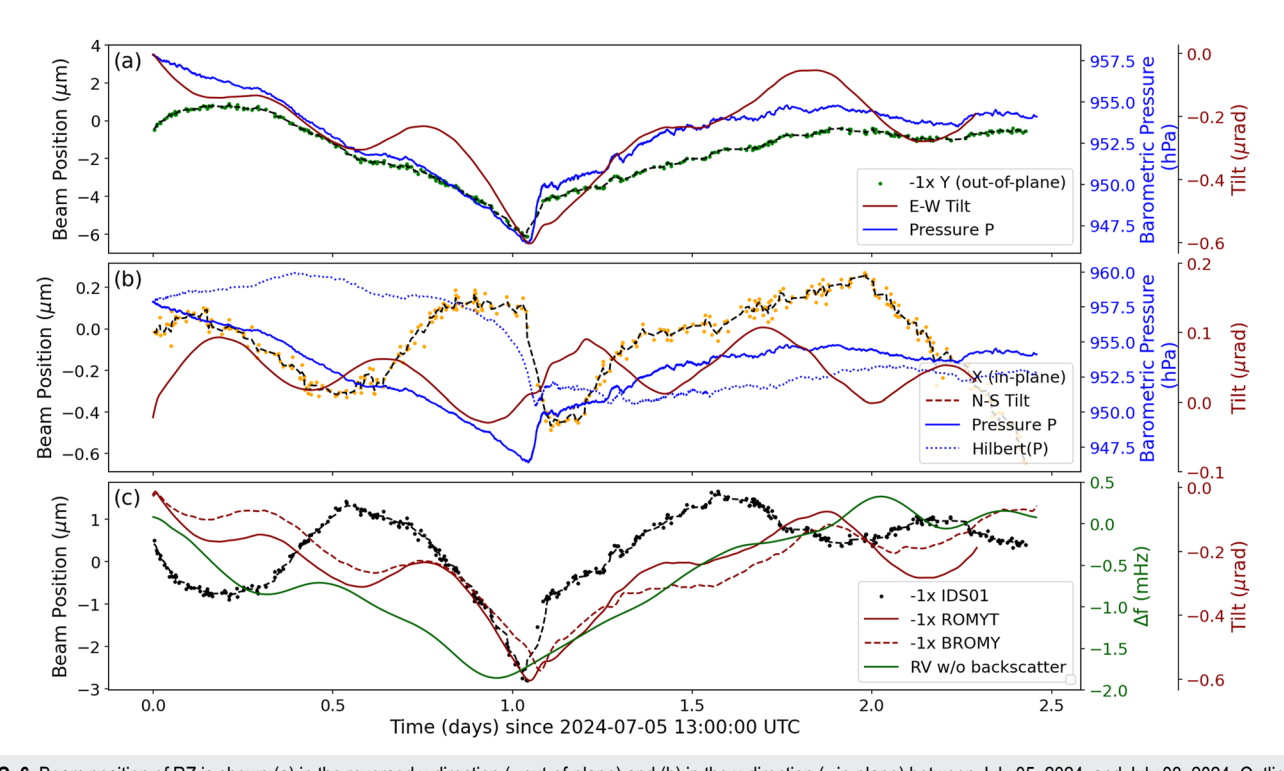


FIG. 6. Beam position of RZ is shown (a) in the reversed y-direction (=out-of-plane) and (b) in the x-direction (=in-plane) between July 05, 2024, and July 08, 2024. Outliers for beam wander were removed. The absolute barometric pressure (blue solid line) and the Hilbert transform of the barometric pressure (blue dotted line) are shown. Tilt observations of the ROMYT tiltmeter located about 50 cm next to the corner are plotted as N–S (red dashed line) and E–W (red solid line) tilts. (c) Comparison of the absolute beam displacement ($\sqrt{X^2 + Y^2}$) of IDS01, the absolute tilt ($\sqrt{N^2 + E^2}$) for ROMYT (solid) and BROMY (dashed) as well as the 6 h moving average of the Sagnac frequency of RV without backscatter.

and temperature control in the future, the hydrologic response, after heavy rain events, may be quantified.

III. DATA ANALYSIS AND CORRECTION

An active RLG, in particular if not geometrically locked, encounters mode jumps and split-mode states. Both may result from the variation of the gain curve or the ORR geometry. The gain power is controlled using an active feedback loop based on the detected monobeam intensity [Fig. 1(a)]. A geometric control system was tested for other RLGs (e.g., Refs. 1 and 19). For ROMY, such a system would require adjustment to the design of the corner boxes and funding to be implemented for four RLGs. By analyzing the deformation dynamics of the system, we provide figures on how to design such a system.

First, we analyze the operational performance of multiple RLGs for an extended observation period based on an automatic recovery system. Next, the enhancement of employing a classic backscatter correction scheme for ROMY's RLGs is presented. Finally, the relation between geometric resonator deformation and external influences is analyzed, modeled, and corrected for using a simple, linear, multivariate regression approach.

A. Operational performance analysis

Split-mode states cause a loss of the Sagnac interferogram. An automatic system detects the absence of the interferogram and launches a recovery procedure, referred to as MLTI (MuLtimode TrIgger). After split-mode state detection, an interruption of the intensity feedback control causes a mode competition regime before reactivating the intensity stabilization and ideally returning to a stable single-mode operation state. If such an operation state is not achieved, another MLTI is launched after 30 seconds. When successful, this restores a single-mode or a stable multimode operation state.

For an operation performance analysis, triggered MLTI launches are logged and used to compute MLTI sequences by merging MLTI launches, which are separated by less than 60 s. After an MLTI sequence, the split-mode operation state is considered successfully resolved. A cumulative percentage count of MLTI sequences in the observational period between September 03, 2024, and July 31, 2024, is shown in Fig. 7(a). Maintenance activity is often required and indicated by yellow vertical bars. A sudden increase in MLTI occurrences is often visible after maintenance activity, mostly related to thermal perturbations. We use the elapsed time between MLTI sequences, referred to as inter-MLTI-time, to describe and quantify the operational stability of the individual rings.

The absolute count of MLTI sequences for RZ amounts to 1821 for this observational period caused by a poorly configured, thus unstable multimode operation state between day 86 and day 102 [see Fig. 7(a)]. RU and RV reveal a similar count of 464 and 443, respectively. A distribution of inter-MLTI-times for RZ shows two pronounced peaks: the first peak at below 1 h is attributed to the mentioned period between day 86 and day 102, and the second specifies the characteristic time between 1 and 2 h. Based on the inter-MLTI-time distribution for RU and RV, their average characteristic time between split-mode operation states is around 6 h [Fig. 7(b)].

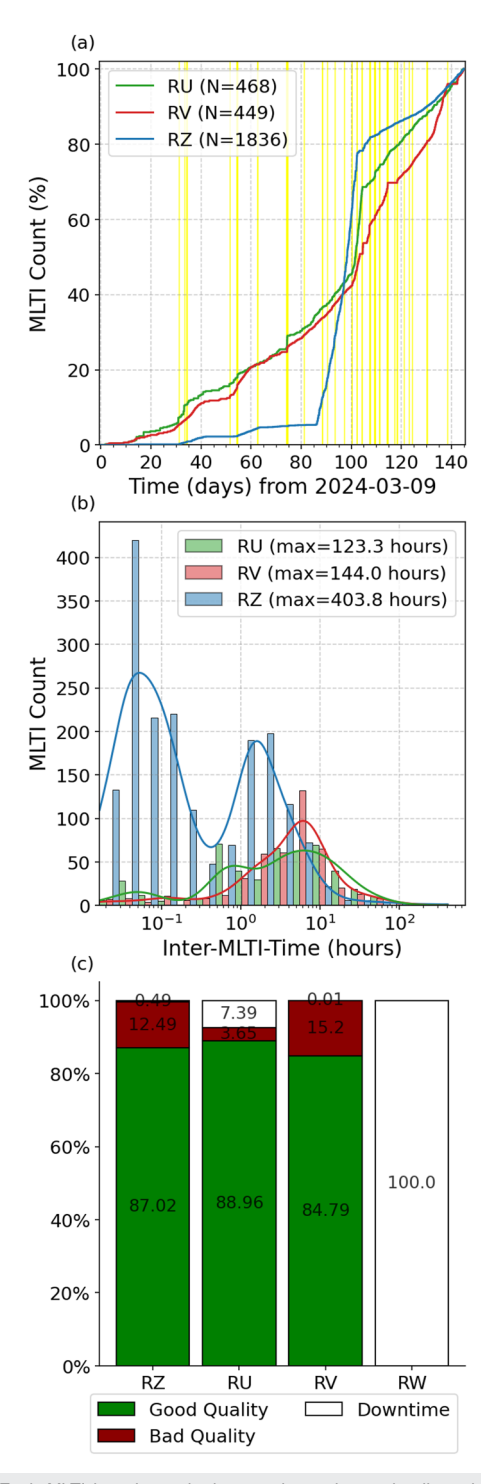


FIG. 7. Each MLTI launch required to resolve a detected split-mode operation state is logged. Statistics for rings RZ (blue), RU (green), and RV (red) between March 09, 2024, and July 31, 2024, are shown. (a) Cumulative percentage count of MLTI sequences. Yellow bars indicate time periods of maintenance activity. (b) Histogram and distribution of inter-MLTI-time (= elapsed time between MLTI sequences). (c) Uptime classified by good (green) and bad (red) quality and downtime (white) in percentage.

The uptime statistic in Fig. 7, being classified as good and bad quality data and non-operation (downtime), is based on a simplified approach presented in Brotzer *et al.*²⁹ and yields for all three operated RLGs comparable good quality uptimes of around 85% [Fig. 7(c)] between March 09, 2024, and July 31, 2024.

Continuous, good quality data on three RLGs are essential to obtain three component rotational ground motions. For the presented example, this comes down to merely 66.2% simultaneously good data quality. Vertical rotation is observed independently by the horizontal ring (RZ). However, for a continuous and stable operation with good quality data, the MLTI count generally has to be minimized and the inter-MLTI-time maximized.

B. Backscatter correction analysis

Backscattered light at the mirrors into the incident monobeam direction causes frequency pulling and pushing, impacting the obtained Sagnac beat frequency by interfering with both monobeams. A correction procedure for these systematic errors was presented by Hurst *et al.*, ³⁰ which is based on the observations of relative monobeam amplitude ratios and their phase relation. Other tested concepts of data processing and backscatter reduction are discussed in the literature. ^{22,31}

In subsequent experiments, we monitored monobeams for each of the operational rings RZ, RU, and RV in order to quantify the contribution of the backscatter effect to the observed Sagnac frequency

drifts. For larger RLGs, generally a smaller backscatter effect is expected, following $L^{-2.5}$ (L = length of the resonator). The signal of the photodiodes is amplified and then transmitted differentially in order to provide a sufficient signal-to-noise ratio [Fig. 1(a)].

An example of the Sagnac frequency time series of RV before and after the backscatter correction (BC) according to Hurst $et\ al.^{30}$ is presented in Appendix F, Fig. 21. A long-term drift for this example across 22 days amounts to 7 mHz, while the short-term variation is within 3 mHz. This is about one order less than observed for the lower performing RU (~10 mHz).

The BC reduces the variation of the Sagnac frequency by about 1 mHz or 2 mHz [Fig. 21(b)]. The achieved variance reduction *R* amounts to 94.5% for the example shown in Fig. 21 of Appendix F. A close-up on two shorter time intervals emphasizes the achieved reduction related to short-term backscatter-induced drifts. The long-term drift remains after the BC, which strongly points toward mechanical instabilities as the dominant error source. A comparable BC reduction is achieved for RZ (see Appendix F, Fig. 22) and RU.

C. Resonator deformation analysis

The ORR includes stainless steel bellows, decoupling the resonator pipes from the three corner boxes [Fig. 1(a)]. For the observed strong changes of the perimeter, the bellows might not be able to take up all the deformation of the entire resonator. A dominant share of deformation, however, occurs at the corner boxes and

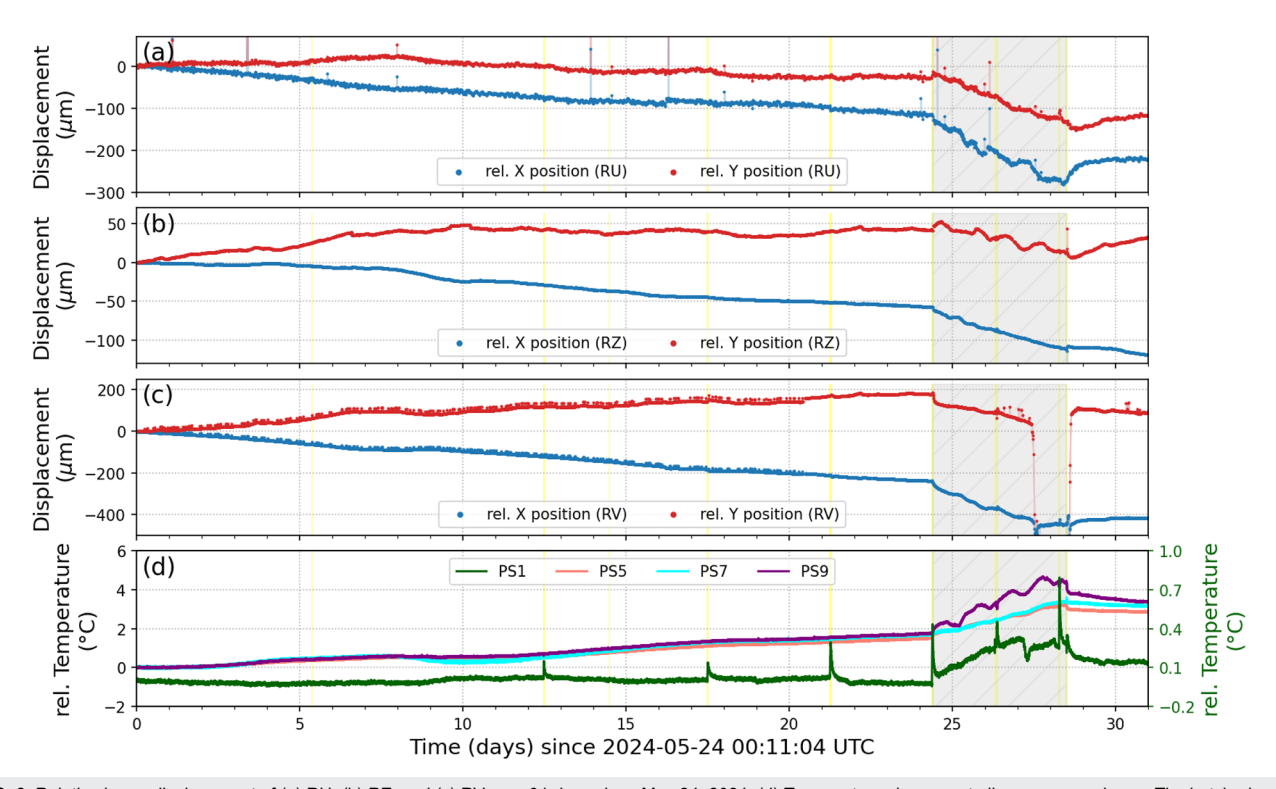


FIG. 8. Relative beam displacement of (a) RU, (b) RZ, and (c) RV over 31 days since May 24, 2024. (d) Temperature changes at all corners are shown. The hatched, gray area marks a time period with activated air ventilation (=strong thermal perturbation). The yellow vertical lines indicate maintenance activity. The beam displacement has a sampling time of 10 min, and outliers have been excluded.

their foundation. Based on slow changes, we further assume that the air temperature in the corner shafts is representative for the mirror corner itself without significant delay.

Geometric deformation at the corner boxes is introduced by thermal expansion and compression and has two origins. First, the concrete monument expands or contracts due to thermal forcing, therefore increasing or decreasing the resonator side length, hence the scale factor [Eq. (3)]. Second, the stainless steel corner boxes, which are designed to minimize thermal deformation onto the mirror position, still contribute to deformation via the alignment lever assembly used to manually align the resonator. However, these two sources of deformation are difficult to separate.

The deformation related to temperature and air pressure variation is analyzed based on an experiment of the horizontal ring (RZ). Three video cameras (IDS01, IDS03, and IDS05) provide beam displacements at two corners during this experiment [see Fig. 1(a)], while an FSR measurement provides perimeter variations.

In a first experiment, we analyze the influence of slow versus fast temperature perturbation on the beam walk for three ORRs (RZ: IDS01 in shaft 07, RU: IDS00 in shaft 09, RV: IDS07 in shaft 07) between May 24, 2024, and June 24, 2024 (Fig. 8). Until day 24, the temperature gradually increases by about 2 $^{\circ}$ C for the records of the upper shafts (PS5, PS7, and PS9), which corresponds to beam displacements in the x-direction of 60 μ m (RZ), 110 μ m (RU), and

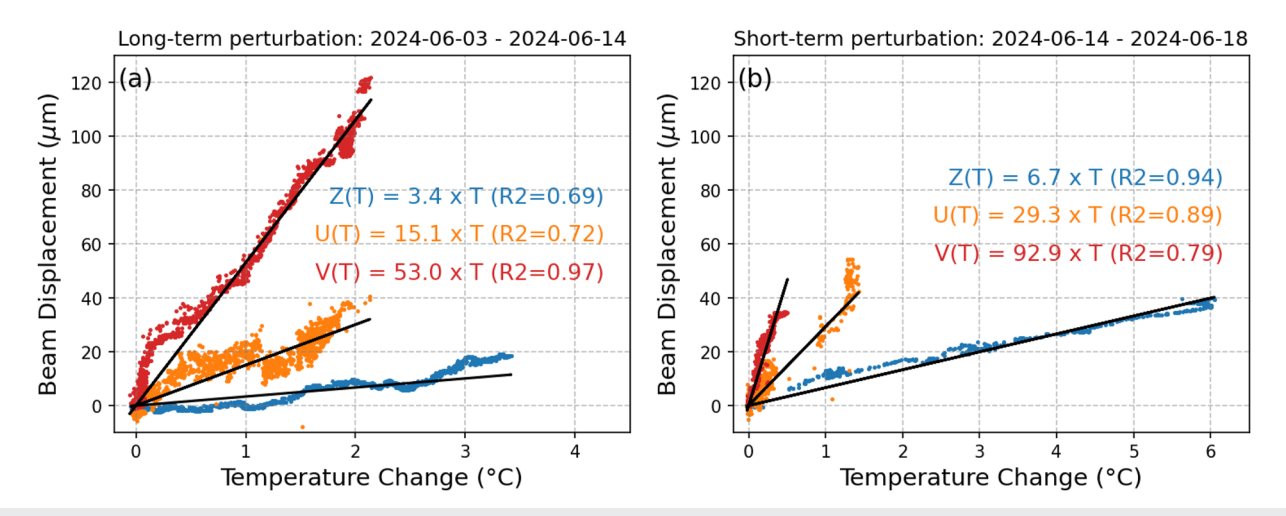


FIG. 9. Linear regression of beam displacement and temperature for RZ, RU, and RV. Absolute beam displacement ($d = \sqrt{x^2 + y^2}$) and combined temperatures at all corners of RU (orange), RZ (blue), and RV (red) during a gradual (a) long-term June 03, 2024, to June 14, 2024, and (b) short-term June 14, 2024, to June 18, 2024, thermal perturbations are used.

TABLE I. Linear thermal coefficients are estimated for different experiments using the RANSAC algorithm based on beam walk (BW) observations at three ORRs (Optical Ring Resonators) for a long-term perturbation (LTP) and a short-term perturbation (STP). For the third experiment with simultaneous perimeter change monitoring (PMM), cameras were mounted at different corners of RZ and the perimeter (PM) was monitored using the FSR measurement. The coefficient of determination R² is listed and represents the fit score

ORR	Absolute BW ($\mu m ^{\circ} C^{-1}$)	\mathbb{R}^2	X — $BW (\mu m ^{\circ}C^{-1})$	\mathbb{R}^2	Y—BW (μ m $^{\circ}$ C ⁻¹)	\mathbb{R}^2	Camera
RZ	6.7	0.94					IDS01
RU	29.3	0.89			•••		IDS00
RV	92.9	0.79	•••		• • •	• • •	IDS07
RZ	3.4	0.69					IDS01
RU	15.1	0.72			•••		IDS00
RV	53.0	0.97	•••	• • •	•••	• • •	IDS07
PM	31.3	0.99					
RZ	13.9	0.95	18.5	0.96	51.3	0.92	IDS01
RZ	12.8	0.94	18.9	0.96	48.3	0.92	IDS03
RZ	9.2	-1.3	2.4	0.47	-32.3	-2.17	IDS05
	RZ RU RV RZ RU RV PM RZ RZ	RZ 6.7 RU 29.3 RV 92.9 RZ 3.4 RU 15.1 RV 53.0 PM 31.3 RZ 13.9 RZ 12.8	RZ 6.7 0.94 RU 29.3 0.89 RV 92.9 0.79 RZ 3.4 0.69 RU 15.1 0.72 RV 53.0 0.97 PM 31.3 0.99 RZ 13.9 0.95 RZ 12.8 0.94	RZ 6.7 0.94 RU 29.3 0.89 RV 92.9 0.79 RZ 3.4 0.69 RU 15.1 0.72 RV 53.0 0.97 PM 31.3 0.99 RZ 13.9 0.95 18.5 RZ 12.8 0.94 18.9	RZ 6.7 0.94 RU 29.3 0.89 RV 92.9 0.79 RZ 3.4 0.69 RU 15.1 0.72 RV 53.0 0.97 PM 31.3 0.99 RZ 13.9 0.95 18.5 0.96 RZ 12.8 0.94 18.9 0.96	RZ 6.7 0.94 RU 29.3 0.89 RV 92.9 0.79 RZ 3.4 0.69 RU 15.1 0.72 RV 53.0 0.97 PM 31.3 0.99 RZ 13.9 0.95 18.5 0.96 51.3 RZ 12.8 0.94 18.9 0.96 48.3	RZ 6.7 0.94 .

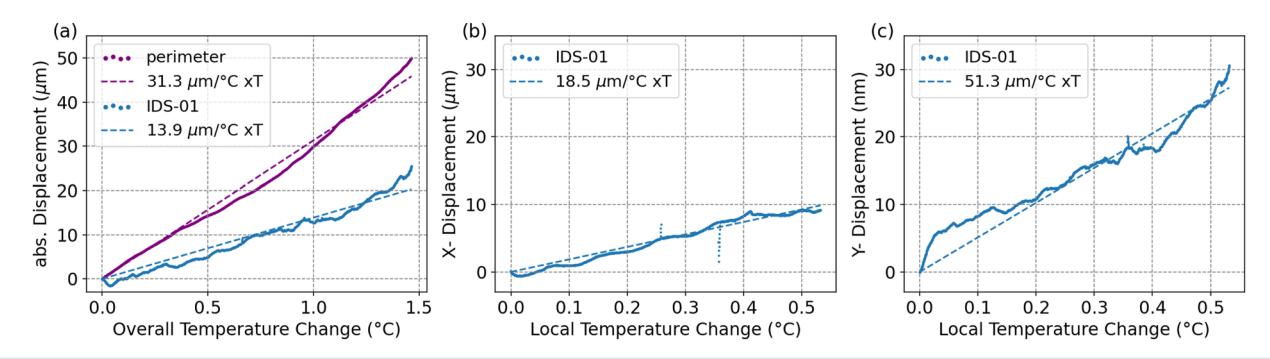


FIG. 10. Thermal linear coefficients are estimated at RZ for (a) the FSR-based perimeter monitoring (purple) and absolute beam walk ($d = \sqrt{x^2 + y^2}$ of IDS01 (blue) using an overall summed temperature record. Panel (b) shows the x-displacement and (c) the y-displacement of the beam walk with IDS01 with the local temperature record in the shaft 07.

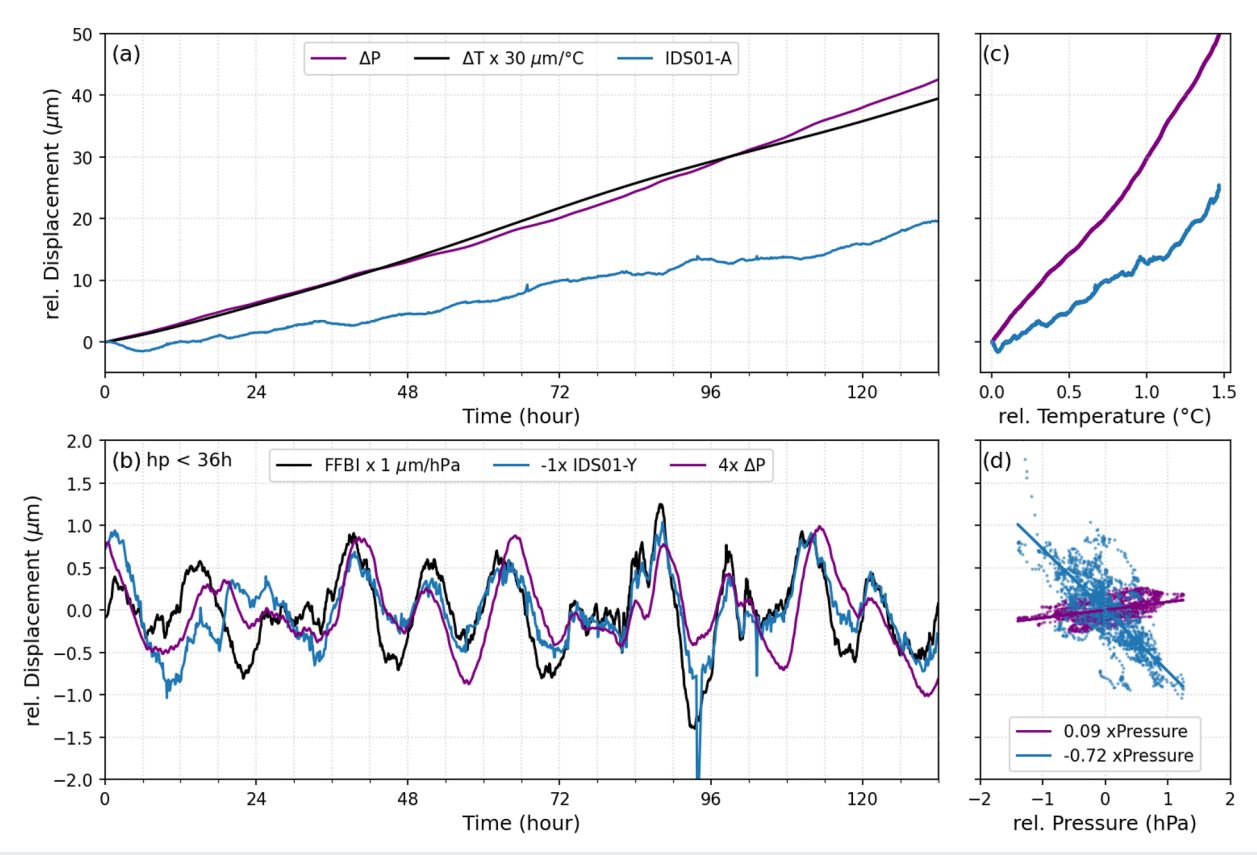


FIG. 11. Separation of external effects on perimeter changes and beam walk at RZ. (a) Relative integrated displacement of the resonator's perimeter (ΔP) based on FSR measurements and absolute beam walk displacement ($\sqrt{X^2 + Y^2}$) for camera IDS01 are compared with combined temperature (black) at all relevant corners (05, 07, 09) scaled by 30 μ m °C⁻¹. (b) High-pass filtered (with a corner period of 36 h) displacements in the y-direction (out-of-plane) with changes in barometric pressure scaled by 1 μ m hPa⁻¹. Note that the perimeter change is scaled by a factor of 4, and the beam walk of IDS01 is inverted. The corresponding scatterplots of displacement vs temperature and barometric pressure change are shown in (c) and (d), respectively. The linear coefficients based on a RANSAC approach with zero intercept are 0.09 and $-0.72~\mu$ m hPa⁻¹.

220 μ m (RV). Air temperature in the central shaft remains stable, except of temperature spikes of short duration during maintenance activity, until an artificial temperature perturbation is introduced between day 24 and day 28 (gray-shaded period) through the activation of the internal air ventilation system inside ROMY (Fig. 8). This introduces a thermal perturbation of 1–2 °C for the upper shafts and about 0.3 °C in the central shaft [Fig. 8(d)]. The immediate response in terms of beam walk at the corners is evident for all three ORRs [Figs. 8(a)–8(c)].

Linear thermal coefficients for the absolute beam displacement $(d = \sqrt{x^2 + y^2})$ are derived for the long-term (LTP: June 03, 2024, to June 14, 2024) and the short-term perturbation (STP: June 14, 2024, to June 18, 2024), as shown in Figs. 9(a) and 9(b), respectively. For the regression, a sum of the temperature records in the three corners of the ORR is used. A linear trend is evident, but modulated by non-linear responses.

The derived linear coefficients based on the RANdom SAmple Consensus (RANSAC) algorithm without an intercept are listed in Table I and reveal that the coefficients for RU and RV are approximately doubled for the artificial short-term thermal perturbation. The different ORRs respond differently to the thermal perturbations, while RV (53.0 and 92.9 μm °C $^{-1}$) shows the strongest response and RZ (3.4 and 6.7 μm °C $^{-1}$) reveals the smallest.

In a second experiment, the perimeter change of RZ was monitored using an FSR measurement, while three cameras monitored beam walk at two corners [see Fig. 1(a)]. The obtained thermal coefficient for the perimeter change is 31.3 μ m $^{\circ}$ C $^{-1}$ (see Fig. 10). The coefficient for the absolute beam walk displacement for IDS01

is less than half with 13.9 μ m $^{\circ}$ C $^{-1}$ compared to the perimeter change, indicating that there is a portion of homogeneous thermal expansion of the resonator not contributing to deformation (=beam walk) at the corner. During the experiment, the dominant temperature increase is observed in shaft 07, explaining a stronger effect on beam displacement observed by IDS01 and IDS03, being located in shaft 07, whereas IDS05 is located in shaft 09.

Peak tracking reveals FSR drift rates of about 20 Hz d⁻¹, which corresponds to a perimeter change rate of about 7 μ m d⁻¹ or 0.115 mHz d⁻¹ in Sagnac frequency variation. The dominant response seems to be attributed to temperature changes, where the increasing combined temperature (at all corners of RZ), scaled by 30 μ m °C ⁻¹ (for visualization purposes), matches this trend [Fig. 11(a)].

After a high-pass filter is applied, both the out-of-plane displacement and the perimeter variation expose a high correlation with barometric pressure changes [Fig. 11(b)], while it is about four times more dominant for the beam walk displacement. Derived linear coefficients amount to 0.09 and $-0.72~\mu m$ hPa⁻¹ for perimeter and beam walk, respectively [Fig. 11(d)].

D. Instrumental response correction

A simple multivariate linear regression approach is employed to model observed beam walk in each direction and the Sagnac frequency drifts based on a set of observables (e.g., temperature and pressure). This is explained in detail in Appendix E. This simple model explains long-term trends and major short-term modulations accurately and supports a dominant effect of temperature on the

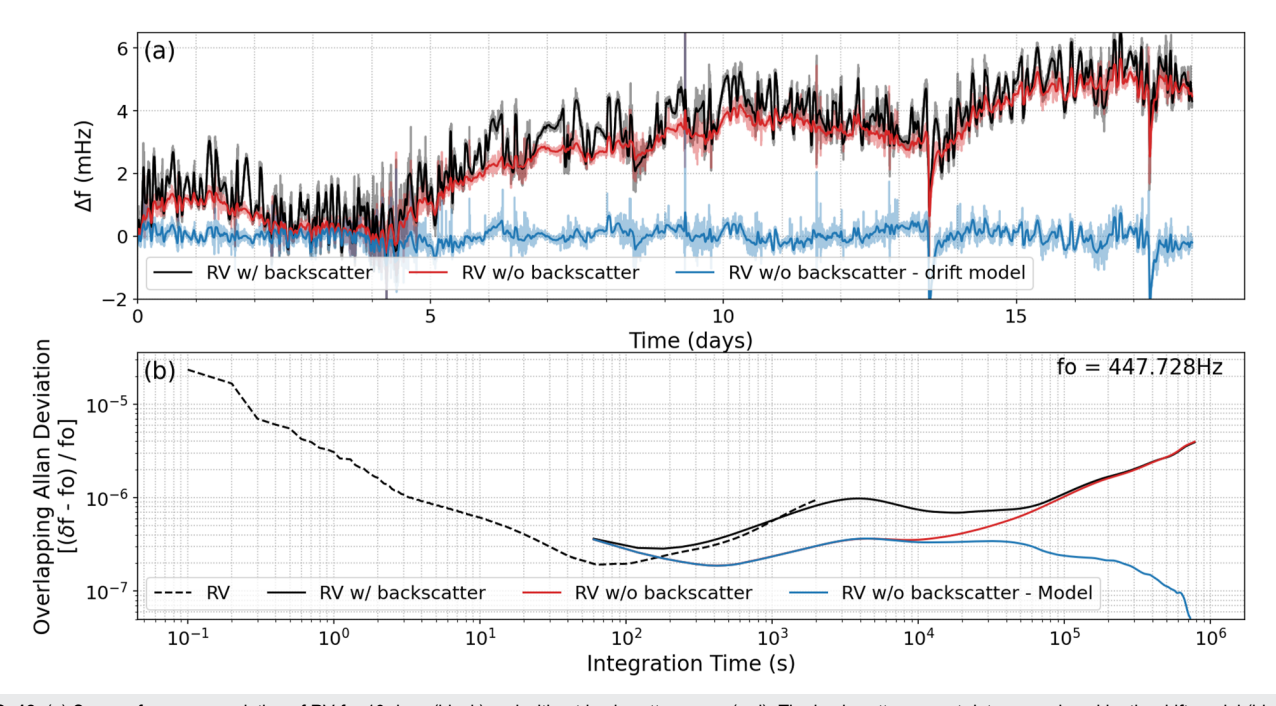


FIG. 12. (a) Sagnac frequency variation of RV for 18 days (black) and without backscatter errors (red). The backscatter correct data are reduced by the drift model (blue). The solid lines represent a moving average of 60 min. (b) Overlapping Allan deviations of the scaled relative Sagnac frequency time series ($\Delta f/f_0$) with $f_0 = 447.728$ Hz. The black dashed line is based on 5 h of 10 Hz data to extend toward smaller integration times.

in-plane and stronger effects of barometric pressure in the out-ofplane direction. The model, however, is incomplete, rendering it incapable of anticipating future deformations. A linear approach is too simplistic to capture all involved processes appropriately.

When computing an Allan deviation for uncorrected data, the minimum is encountered at about 100-200 s. After applying the BC, the minimum is shifted toward 400 s. Using the multivariate linear mode to correct drifts in the backscatter-corrected Sagnac frequency time series yields an improved Allan deviation, for integration times above 10^4 s (Fig. 12).

The currently available dataset limited to 18 days does not allow inferring general long-term reduction success, but indicates the potential and an improved understanding of the dominant influences. A more complex model would be required to fully capture all deformation effects. Instead of the model based correction during post-processing, we rather suggest active control systems to stabilize the geometry of each ORR.

IV. DISCUSSION

The heterolithic realization of the ROMY structure near the surface naturally poses challenges with regard to the mechanical stability of the optical resonators. External influences (e.g., temperature and barometric pressure) cause instrumental effects by altering the scale factor and/or orientation of the RLGs and have to be understood. The actual rotation rate induced by external forces (e.g., atmospheric pressure to ground coupling) is expected to contribute to the signal but is not currently dominant. Quantifying these influences helps mitigate or correct the instrumental effects and enhance the operational stability toward continuous high-quality data acquisition.

Uncorrected Sagnac beat frequency time series exhibit long-term drifts in a range of several tens of mHz over 5 months, indicating mechanical instability of the ORRs. The observations of an instrumental response to temperature and pressure changes by the RLGs of ROMY motivated to better quantify and understand the underlying effects. For this study, a monitoring network was designed and implemented. An implemented passive thermal insulation reduces daily and sub-daily effects, but not seasonal temperature fluctuations inside the upper access shafts. In order to mitigate this long-term trend, an active temperature control system has to be implemented.

Three RLGs were successfully operated for an extended observation period with good quality data. The operational performance analysis over several months reveals frequent occurrence of split-mode states and resonator misalignment, often linked to thermal perturbation introduced during maintenance activity. Based on inter-MLTI-times, RU and RV appear to have a higher operational stability at around 6 h compared to RZ [Fig. 7(b)]. In the future, more stability is required for continuous geoscientific observations for all three rotational components.

The BC achieves short-term drift reduction in the 1–2 mHz range. For smaller, heterolithic RLGs, such as the ER-1³² or GIN-GERino,²³ the backscatter introduced error is larger, amounting to 50–90 mHz or -25 to 30 mHz, respectively. The backscatter-induced effects for ROMY are stronger than expected for a RLG of 12 m side length. This likely results from beam divergence over the long arms

and an increased beam diameter that illuminates more of the mirror, resulting in more (back)scatter than expected. Scattered light, due to illuminating the capillary of the gain tube, might additionally contribute. The detection of weak monobeam signals to apply the BC is challenging in the presence of relatively strong electronic hum noise, but is required for all four RLGs for geodetic signal analysis in the future.

Remaining long-term drifts in the backscatter-corrected data are dominated by external influences of ambient temperature and barometric pressure on the geometry and orientation of the ORR. On the one hand, the common concrete monument of the corners in the shafts experiences deformation, while on the other hand, the stainless-steel corner boxes and their alignment controls are affected directly. Deformation of the controls acts via a lever and is expected

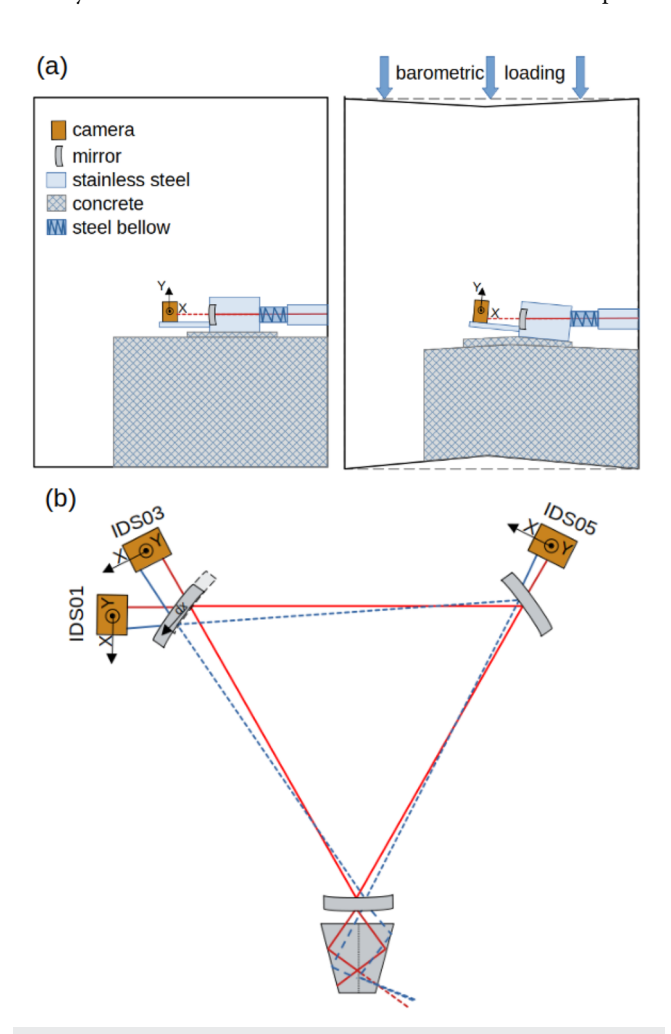


FIG. 13. (a) Schematic deformation of the schematic access shaft and monument due to barometric loading at the top, resulting in an out-of-plane beam displacement recorded by the y-direction of the camera (orange square). (b) Schematic in-plane beam displacement due to mirror deformation. The upper left mirror is displaced in this example, causing the formerly red beam plane to adjust to the blue dashed beam plane. This also affects the beam combination in the Koesters prism at the bottom corner, thereby impacting the interferogram quality. Sketches are exaggerated and not to scale.

to be the dominant source of deformation. However, it is extremely difficult to observe these effects separately.

Deformation at the corner boxes can be detected and quantified in an out-of-plane and in-plane direction using beam walk observations with video cameras. Beam displacements in a range of 100 and 340 µm for the out-of-plane and in-plane directions, respectively, are observed for RU over 74 days (Fig. 3).

Inferred linear thermal coefficients differ for the RLGs and typically range in the tens of micrometer displacement per degree Celsius for different experiments. Hence, thermal deformation at the corners has a strong effect on the geometry and orientation of the beam plane and is thus responsible for pronounced instrumental effects. Strong temperature perturbations might promote non-linear behavior. For slower, more gradual temperature variations, inferred thermal coefficients are about half as large as for strong, short-term perturbations. With regard to FSR inferred perimeter changes, about half of the thermal expansion contributes to deformation at the corner and the monument, which is captured in absolute beam walk, whereas the other half seems to be homogeneous (or symmetrical) expansion at the corners, contributing only to the change in perimeter.

The schematic model presented in Fig. 13 illustrates the deformation acting in-plane and out-of-plane separately. In-plane deformation at the mirrors affects the beam plane geometry and affects the scale factor, as well as the combination of the beams, thereby impacting the interferogram quality or contrast [Fig. 13(b)].

Thermal strain of one optical wavelength along the resonator can be related to mode jumps. The inferred linear thermal expansion coefficients are comparable to common values for concrete²⁶ or structural steel.²⁷ As mode transitions may result in split-mode operation states, this affects the operational stability and has to be mitigated.

Exemplary barometric events cause a response of the Sagnac frequency (Fig. 6). Barometric pressure and out-of-plane beam displacement show a high correlation, while a reduced effect is found for the observed perimeter change. A response is also observed on the inertial tiltmeter, which is why we attribute this deformation to a local cavity effect, as discussed by Zürn *et al.*²⁸ The local barometric loading/unloading at the surface deforms the cylindrical corner shaft, representing an underground cavity, in a way that the resonator corner deforms dominantly along the out-of-plane degree-of-freedom, as illustrated in Fig. 13(a). In-plane beam displacement is roughly one order of magnitude smaller and does not reveal a clear correlation. An in-plane deformation is not expected for the vertically acting loading due to barometric pressure.

Variations of the near-surface hydrology causing asymmetric hydrostatic pressure changes are expected to have an effect on the orientation and possibly also internal deformation of the ROMY structure. At this stage, however, these effects are obscured by more pronounced effects, such as ambient temperature and air pressure.

A simple, linear multivariate model is able to model the long-term drifts observed in the Sagnac frequency time series of RV. These modeled instrumental drifts can be used as a drift correction and improve the long-term stability, expressed by a reduced Allan deviation toward integration times of several days. As the underlying relations are oversimplified in this linear model, a more complex correction model is required. Corrections during post-processing,

however, do not improve the operational stability, which is why implementing an active stabilization system for the ORRs of ROMY is recommended.

V. CONCLUSIONS

The RLG array ROMY is currently the only RLG array that can provide all three components of rotation for geoscientific observations at high sensitivity. The heterolithic realization of the ROMY structure near the surface creates a susceptibility to external influences (e.g., temperature and barometric pressure), compromising the mechanical stability of the RLGs. Geodetic observations require mechanical long-term stability, while for seismological observations, a continuous operation without mode jumps and split-mode occurrences is essential. The operation of multiple RLGs with uptime above 80% is feasible with high maintenance effort to avoid misalignment of the ORRs.

The geometric deformation caused by temperature and barometric pressure on the ORR was monitored and analyzed. Scale factor alteration by the changes in size and orientation are dominated by thermal extension and contraction of the corner mirrors via the corner boxes and the monument. A smaller effect on the geometry, in particular the orientation of the beam plane, is caused by deformation introduced by barometric loading.

Observed deformation of tens to hundreds of micrometers result in strong drifts of the Sagnac frequency and have to be mitigated for an enhanced and continuous operation. This requires a sophisticated, active, control system stabilizing both degrees-of-freedom at the corner boxes. This might be feasible by stabilizing the perimeter via an FSR-referenced feedback loop. A geometric locking system as employed for the heterolithic RLG GP2 ¹⁹ is not adoptable for the ORRs inside the large concrete structure of ROMY. Orientation changes due to deformation in the out-of-plane direction, which are not entirely captured by perimeter changes, might require a different approach, potentially using beam walk monitoring.

The installed passive thermal insulation successfully avoids strong daily and sub-daily variations. In order to mitigate seasonal variations in temperature inside the upper shafts, an active temperature control system is required. Barometric pressure control with the current structural design is not realizable.

Toward geodetic observations, all four RLGs require monobeam observations to apply backscatter correction and reduce short-term frequency drifts by about 1–2 mHz. In order to eventually exploit ROMY's full potential as the only multicomponent, high-sensitive ring laser array for geodetic signals (e.g., polar motion or length of day variations) with a theoretical resolution of 10^{-13} rad s⁻¹, more effort has to be invested to increase the long-term stability, eventually toward weeks and months (> 10^{5} s integration time).

ACKNOWLEDGMENTS

We gratefully acknowledge the support from the European Research Council for funding the ERC-Advanced ROMY Project (Grant No. 339991). We acknowledge the research funding and support of the faculty of geosciences of the Ludwig-Maximilians Universität München, Germany. Computing resources are funded by the Deutsche Forschungsgemeinschaft (DFG, German Research Foundation)—No. 518204048. We acknowledge technical equipment for experimental setups provided by the Quantum Metrology Group of the University of Bonn, Germany. We thank K. Maetschke for contributing to the ROMY illustration in Fig. 1(c). Continuous technical support from the staff at the Geophysical Observatory in Fürstenfeldbruck, namely, J. Loos, M. Teerporten and S. Egdorf, is highly acknowledged.

AUTHOR DECLARATIONS

Conflict of Interest

The authors have no conflicts to disclose.

Author Contributions

Andreas Brotzer: Conceptualization (equal); Formal analysis (equal); Investigation (equal); Methodology (equal); Project administration (equal); Software (equal); Validation (equal); Visualization (equal); Writing – original draft (equal); Writing – review & editing (equal). Heiner Igel: Conceptualization (equal); Funding acquisition (equal); Resources (equal); Supervision (equal); Writing – review & editing (equal). Felix Bernauer: Conceptualization (supporting); Investigation (supporting); Resources (supporting); Validation (supporting); Writing – review & editing (supporting). Joachim Wassermann: Investigation (equal); Resources (equal); Validation (equal); Writing – review & editing (equal). Jan Kodet:

TABLE II. Video cameras used for beam tracking by IDS Imaging Development Systems with model type, sensor size, and resolution specifications. RLG and shaft, by means of cardinal direction, specify at which ring resonator and access shaft the camera was deployed.

Code	Model	Sensor size (H x W)	Pixel size (μm)	Resolution (MPx)	RLG	Shaft
IDS00	UI-1240LE-NIR-GL	2748 × 3840	1.67	10.0	RU	NW
IDS01	UI-1490LE-M-GL	1024×1280	5.30	1.31	RZ	S
IDS03	UI-1490LE-M-GL	1024×1280	5.30	1.31	RZ	S
IDS05	UI-1490LE-M-GL	1024×1280	5.30	1.31	RZ	NW
IDS07	UI-1490LE-M-GL	1024×1280	5.30	1.31	RV	S

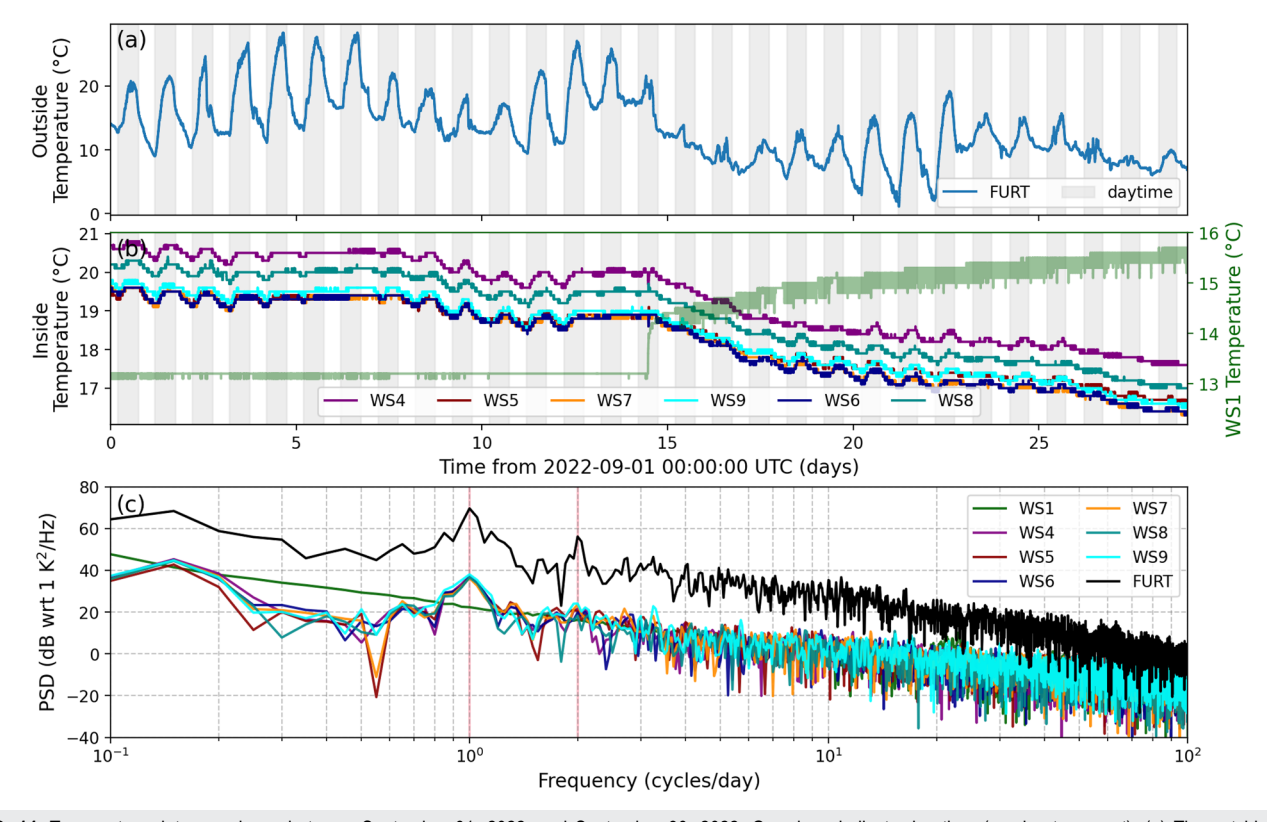


FIG. 14. Temperature data are shown between September 01, 2022, and September 30, 2022. Gray bars indicate day time (sunrise to sunset). (a) The outside air temperature recorded at the weather station FURT. (b) Air temperature records of sensors inside ROMY's shafts. In (c), power spectral density is shown for each outside (FURT) and inside (WS) measurements based on the time series in (a) and (b), respectively.

Methodology (supporting); Resources (equal); Writing - review & editing (equal). Karl Ulrich Schreiber: Conceptualization (equal); Funding acquisition (supporting); Methodology (supporting); Supervision (supporting); Validation (supporting); Writing review & editing (equal). Jannik Zenner: Resources (equal); Writing - review & editing (equal). Simon Stellmer: Conceptualization (supporting); Methodology (supporting); Resources (supporting); Validation (supporting); Writing – review & editing (equal).

DATA AVAILABILITY

Ring laser data of ROMY were provided by the Geophysical observatory in Fürstenfeldbruck.³³ Extensive parts of data processing were done using modules of the ObsPy Python package.34 All other data used in this paper came from published sources listed in the references. Processed data, data processing scripts, and Jupyter Notebooks to create the figures are accessible at the following repositories. For more details, please contact the corresponding author. Online Repository at: https://syncandshare.lrz.de/getlink/ fiN8s26Zjy4bSoQBA9hSyF/RSI-ROMY-2024. Github repository at: https://github.com/andbrocode/InstrumentalEffectsROMY.git.

APPENDIX A: IDS CAMERA TABLE

Table II lists the video cameras used for beam tracking by IDS Imaging Development Systems with model type, sensor size, and resolution specifications. The RLG and shaft, by means of cardinal direction, specify at which ring resonator and access shaft the camera was deployed.

APPENDIX B: VARIANCE REDUCTION

The variance reduction R (in percent) between signal variance σ_{sig}^2 and residual variance σ_{res}^2 is defined by

$$R = \frac{\sigma_{sig}^2 - \sigma_{res}^2}{\sigma_{sig}^2} \times 100.$$
 (B1)

APPENDIX C: PASSIVE THERMAL INSULATION

Thermal stability is essential to improve the operational stability of the heterolithic RLGs of ROMY, as described in Secs. II D and III C. The observed temperature variations (°C down to m°C) have a significant effect on the scale factor (see Fig. 5 or Fig. 16). In order to reduce observed temperature variations inside ROMY's shafts, a passive thermal insulation was designed and installed.

The passive thermal insulation intends to provide more stable temperature conditions by (1) suppressing air mass exchange between outside and inside by introducing a low conductive barrier

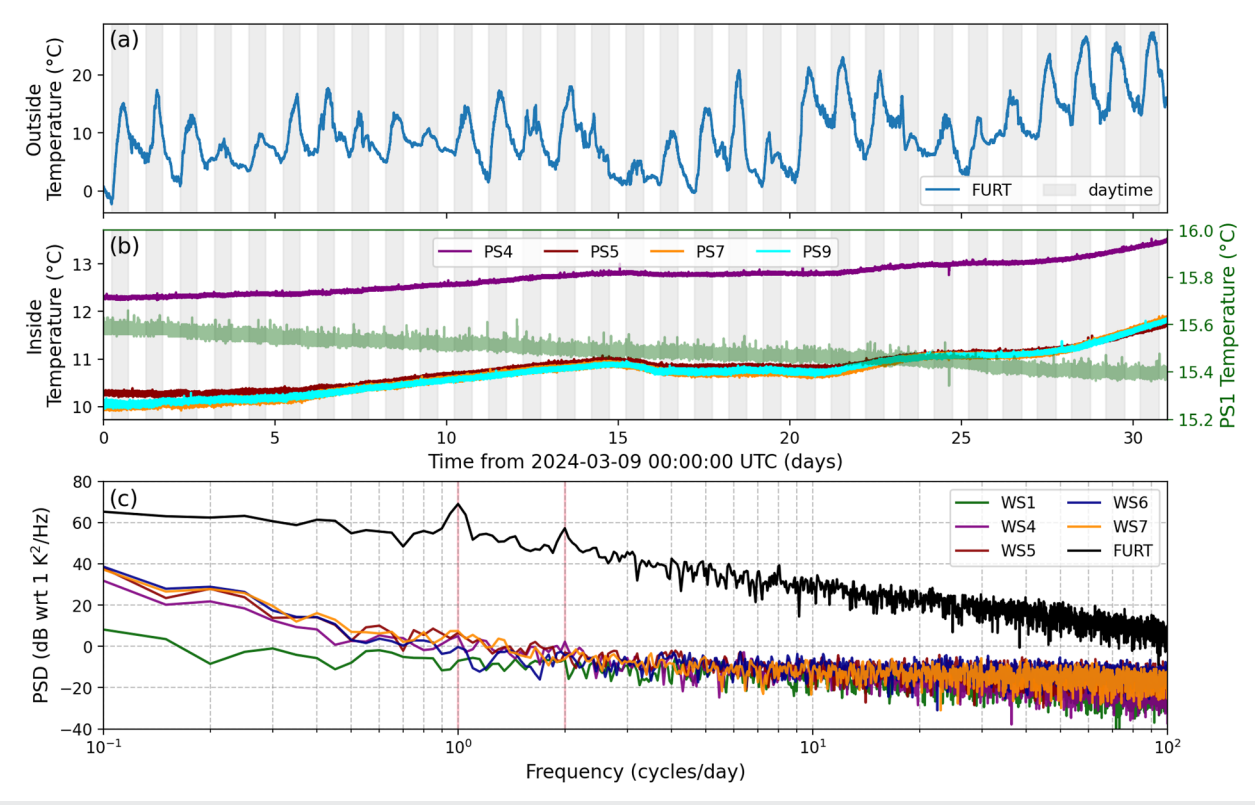


FIG. 15. Temperature data are shown between March 09, 2024, and April 09, 2024. Gray areas indicate day time (sunrise to sunset). (a) The outside temperature recorded at the weather station FURT. (b) Temperature records of five DPS310 sensors inside ROMY's shafts. (c) Power spectral densities are shown for DPS310 and FURT records based on the time series in (a) and (b).

and (2) limiting strong air convection to the upper volume near the exposed metallic cover, experiencing strong heat intake.

A 60 mm thick styrofoam plate is mounted on a sliding aluminum frame to separate the smaller, upper volume from the main volume containing the resonator corners. The sliding system is installed at the ceiling of the shaft. This design can be considered as a low-pass filter to reduce daily and sub-daily air temperature fluctuations. In addition, an electrically rotatable valve was installed for the ventilation pipe of the central shaft to automatically close this direct link, avoiding ambient temperature fluctuations to enter, unless maintenance work is being conducted.

To verify the enhancement, observations before and after the installation of the insulation are provided in Figs. 14 and 15, respectively. Outside air temperature observations in September 2022 [Fig. 14(a)] contain many days with strong daily variations of more than 10 $^{\circ}$ C, also reflected as pronounced spectral peaks in Fig. 14(c) at one and two cycles per day.

With no thermal insulation, except of closed metallic top covers, the temperature variations propagate inside the shafts, visible in the time and frequency domains, especially by a broad spectral peak at one cycle per day. Temperature sensors WS4 and WS8 are located in access shafts that host electronics for plasma discharge, and elevated absolute temperature levels in these shafts are most

likely related to electronic excess heat. Sensor WS1 is located at the bottom of the central shaft at a depth of about 14 m below surface, with the most stable temperature conditions at about 12–16 $^{\circ}\mathrm{C}$ throughout the year.

If present, any daily or sub-daily air temperature variations for WS1 are below the sensor resolution threshold. The sudden increase in air temperature on day 14 [Fig. 14(b)] is linked to automatic activation of a dehumidifier unit, which is also reflected in the corresponding power spectral density.

The insulation is fully operational since 2024-03-09. The impact of the passive, thermal insulation is tested by comparing the period before the insulation (Fig. 14) and a period without major maintenance activity after all insulation plates were installed (March 09, 2024–April 09, 2024).

Outside air temperature for this period in spring shows comparable variations as before in September [Fig. 15(a)]. Inside temperature is based on the records of upgraded sensors located in five access shafts (01, 04, 05, 07, and 09). Being at the bottom of the central shaft, PS1 represents again the most stable air temperature between 15.4 and 15.6 °C. Daily or sub-daily air temperature variations are, however, not visible in the time series nor the power spectra. At the daily and sub-daily spectral peaks, the difference between outside and inside is \sim 50 dB.

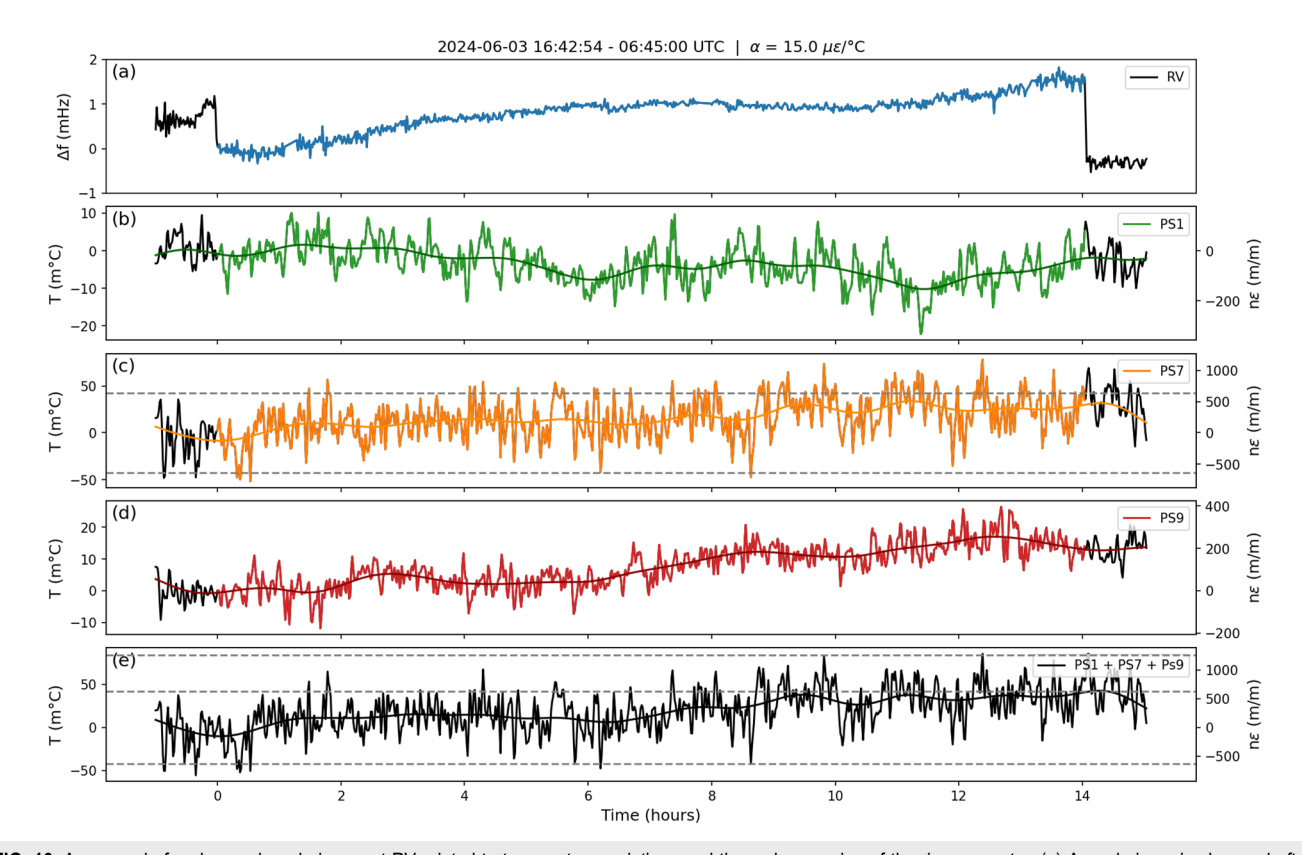


FIG. 16. An example for observed mode jumps at RV related to temperature variations and thermal expansion of the ring resonator. (a) A mode jump is observed after \sim 14 h for the relative Sagnac frequency of RV. (b)–(d) Air temperature measurements in the corner shafts 01, 07, and 09 of ROMY. (e) A superposition of the individual temperatures. Each temperature has a strain axis showing converted temperature to linear strain using a thermal expansion coefficient of $\alpha = 10 \ \mu \ \epsilon/^{\circ} C$.

We find that the passive thermal insulation successfully acts as a low-pass filter, suppressing short-term variations. In turn, this reduces thermal forcing on the ring resonators, thereby minimizing instrumental effects and drifts, and improves the short-term operational stability. The upper shafts still show a slow long-term temperature increase. The passive insulation, however, cannot mitigate seasonal variations (Fig. 15).

APPENDIX D: TEMPERATURE VARIATION AND MODE JUMPS

Within the Sagnac frequency time series, we observe frequent mode jumps not causing split-mode states but shifting the Sagnac frequency. An exemplary mode jump is shown in Fig. 16(a), occurring after about 14 h, shifting the Sagnac frequency of RV by about 2 mHz.

Assuming that a mode-jump occurs when the perimeter of the ORR is expanded (or contracted) by at least one wavelength (\simeq 633 nm), we can estimate linear thermal expansion coefficients. In order to study the temperature variation only, we have to assume that no other environmental effects act on the Sagnac frequency at the same time. Most thermal deformation is assumed to accumulate

at the corners of the triangular ORR, based on the decoupling provided by stainless steel bellows. The air temperature measurements inside the three corner shafts (01, 07, and 09) of the ORR of RV as well as a summed (=overall) temperature trace are shown in Fig. 17.

In order to accumulate a linear strain along the resonator perimeter of about 633 nm, a linear thermal expansion coefficient of α = 15 μ $\epsilon/^{\circ}C$ has to be used. In this example, most temperature variation, hence strain, is attributed to the corner in shaft 07. An expansion of the rORR as a result of an increase in temperature causes an increase in the enclosed area and perimeter and, thus, in the Sagnac frequency [Eq. (1)], as seen in Fig. 16(a).

A second example with a sequence of five mode jumps, with a rather constant repetition time of ~2 h, is shown in Fig. 16(a) for RV. Before and after this sequence, a split-mode operation state occurs. Between the mode jumps, the Sagnac frequency shows an increasing trend, which does not meet the expectations for an overall decreasing temperature trend, namely a contraction of the resonator. From the start of the sequence to the end, however, we find an overall decrease in Sagnac frequency, in accordance with expectations. For an α of 10 μ ϵ /°C, an integrated strain of 633 nm is obtained between the split-mode states with regard to the overall temperature (Fig. 17). We cannot explain the intermediate mode jumps comprehensively.

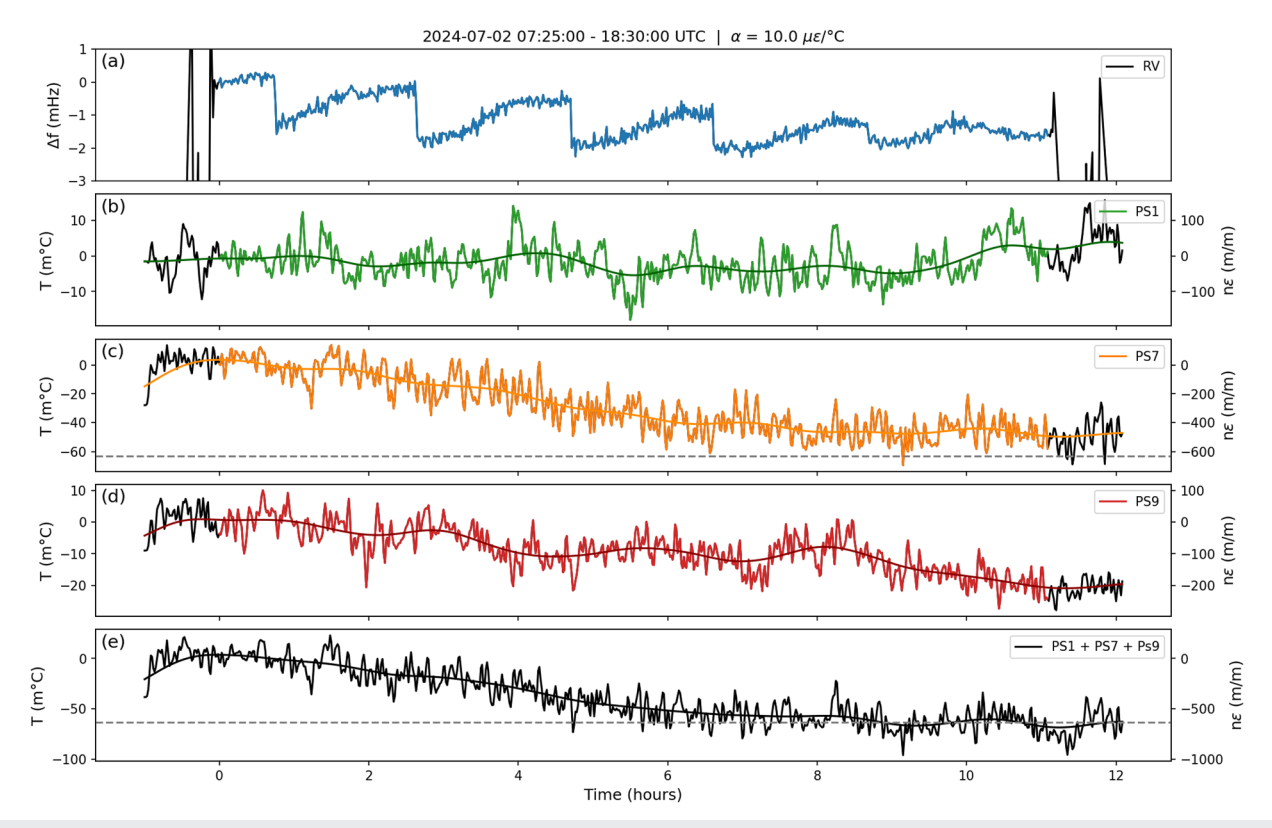


FIG. 17. An example for observed mode jumps at RV related to temperature variations and thermal expansion of the ring resonator. (a) Over 12 h five mode jumps are observed for the relative Sagnac frequency of ROMY's western ring (RV). (b)–(d) Air temperature measurements in the corner shafts 01, 07, and 09 of ROMY. (e) A superposition of the individual temperatures. Each temperature has a strain axis showing converted temperature to linear strain using a thermal expansion coefficient of $\alpha = 15 \mu \varepsilon/^{\circ}$ C. The gray dashed lines represent multiples of 633 nm. Moving averages are shown for the temperature measurements in order to better visualize the trend.

The estimated thermal coefficients of 10 $\mu \, \varepsilon$ /°C to 15 $\mu \, \varepsilon$ /°C are similar to commonly used values for concrete (8 $\mu \varepsilon$ / $^{\circ}$ C to 13 $\mu \varepsilon$ / $^{\circ}$ C; Eurocode 2; Bamforth et al.²⁶), which can vary strongly depending on the used concrete aggregate. Structural steel is based on similar values (10 $\mu \varepsilon$ / $^{\circ}$ C to 12 $\mu \varepsilon$ / $^{\circ}$ C; Eurocode 3, Ref. 27).

APPENDIX E: INSTRUMENTAL RESPONSE MODELING

We employ a simple multivariate regression analysis to model and correct beam walk (bw) and Sagnac frequency data,

$$bw = \sum_{n} c_n Q_n, \qquad (E1)$$

with c_n being the linear coefficients and Q_n being the observed driving quantities. The Kendall rank correlation serves as a measure of dependence between pairs of observables. The linear regression is based on a RANSAC (RANdom SAmple Consensus) algorithm, which is a robust regression approach that automatically identifies and rejects outliers, as expected, for example, due to maintenance

An example model for bwy and bwx based on the data of RV is presented in Figs. 18(a) and 18(c), respectively. Here, the first two-thirds of the dataset (gray-shaded) are used to determine linear coefficients for each model with a subset of observables based on their Kendall rank correlation,

$$bwy = c_0 \cdot bdo + c_1 \cdot ps1 + c_2 \cdot ps7 + c_3 \cdot ps9 + c_4 \cdot mae + c_5 \cdot man,$$

 $bwx = c_0 \cdot ps1 + c_1 \cdot ps7 + c_2 \cdot ps9 + c_3 \cdot mae + c_4 \cdot man,$

with the abbreviations of observables listed and described in Table III. The observables are smoothed using a moving average of 30 min and reduced by the start value.

The modeled beam walk (light red) captures the long-term trends and major, short-term modulations well (Fig. 18) with an overall R² value of 0.99. Generally, the simple multivariate linear model reproduces the observed dominant drifts well, which supports that the included observables are, indeed, main drivers for the deformation. A dominant effect of temperature on the in-plane (bw_x) direction and stronger effects of barometric pressure on the out-of-plane (bw_v) direction are supported by the model.

The predicted beam walk (purple), based on the obtained linear model coefficients, deviates significantly from the observation (black), which indicates an oversimplified model (Fig. 18), which might be due to non-linear (e.g., hysteresis) effects, contributing to the response of the ORR or the concrete foundation. The simple model is not able to handle sudden changes (e.g., temperature spikes

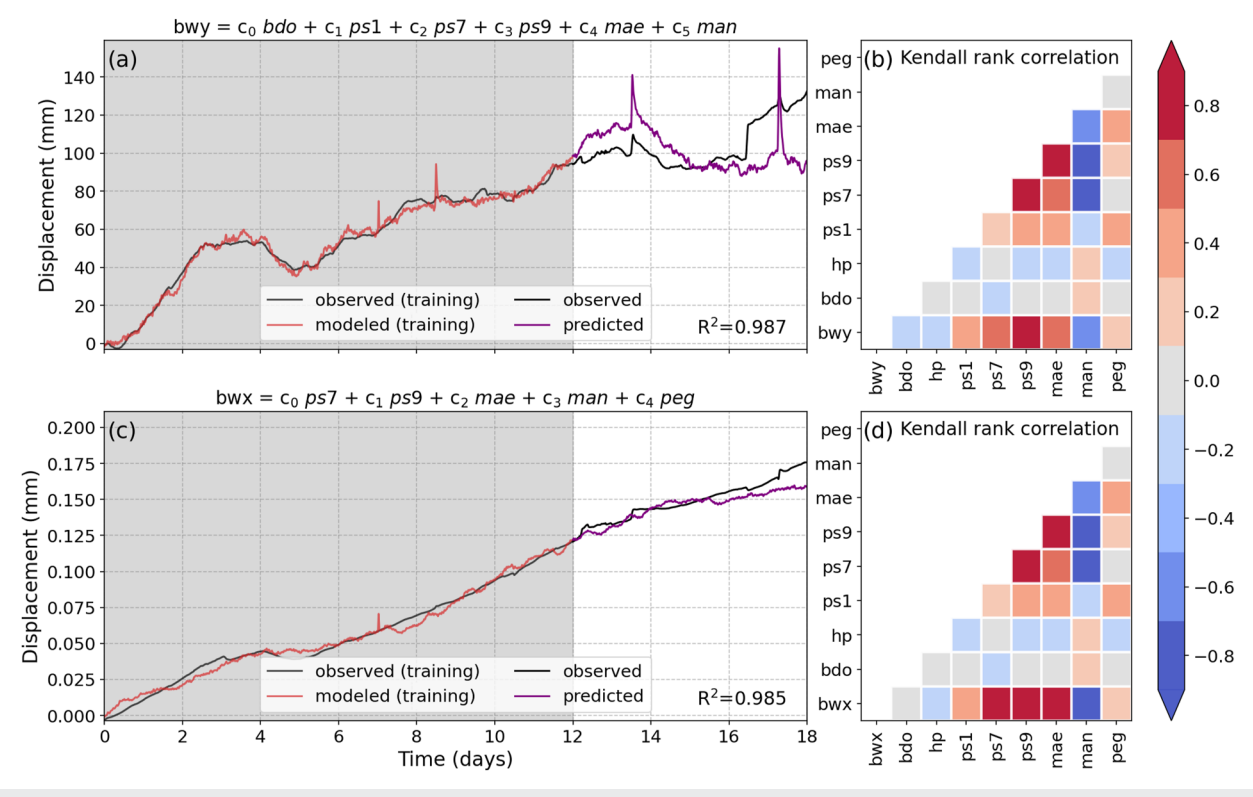


FIG. 18. Time series of the relative beam displacement for RV are shown (a) in the x-direction (bmx, in-plane) and (c) in the y-direction (bwy, out-of-plane) as observed (black) and modeled (red). Data in the gray shaded area are used to fit a linear, multivariate model as defined on top. The prediction (purple) is based on the obtained model coefficients. Kendall rank correlation coefficient matrices are shown in (b) and (d) for bwy and bwx, respectively. The observables are peg = water level, man = N-S tilt, mae = E-W tilt, ps1|ps5|ps9 = air temperature inside shaft 1|5| 9, bdo = absolute air pressure, and hp = Hilbert transform of air pressure.

TABLE III. Code used for quantities, the unit, and a quantity description are provided. C_n are linear coefficients obtained using a multivariate model based on a RANSAC regression algorithm.

Parameter	Unit	$C_n(bwx)$	$C_n(bwy)$	$C_n(fs)$	Description	
fsbs	mHz				Sagnac frequency with backscatter correction	
bwx	μm			0.06	x-displacement on ids07	
bwy	μm			0.001	y-displacement on ids07	
peg	m			-0.1	Groundwater level	
man	μ rad	-3.1	4.6	1.1	N-S tilt of station ROMYT	
mae	μ rad	9.9	24.9	0.4	E-W tilt of station ROMYT	
ps1	°C	319.6	223.1	-0.8	Air temperature in shaft 01	
ps7	°C	-14.2	-39.4	2.7	Air temperature in shaft 07	
ps9	°C	115.7	82.6	-4.8	Air temperature in shaft 09	
bdo	hPa		-2.6	0.1	Absolute barometric pressure at station FFBI	
hp	hPa	•••	•••	• • •	Hilbert transform of barometric pressure	

introduced during maintenance activity). Furthermore, the observables are not entirely independent, which is reflected by a higher Kendall correlation between the observables, not merely with respect to *bwy* and *bwx* [Figs. 18(a) and 18(b)].

In a next step, we use the simple, linear, multivariate regression approach to model drifts of the Sagnac frequency directly, taking into account a set of observables, including beam walk (*bwx* and *bwy*), air temperature (*ps7* and *ps9*), and barometric pressure (*bdo*), as well as the Hilbert transform of the barometric pressure (*hp*),

$$\delta f = c_0 \cdot bwx + c_1 \cdot bwy + c_2 \cdot ps7 + c_3 \cdot ps9 + c_4 \cdot bdo + c_5 \cdot hp.$$

Hereby, the observables are smoothed using a moving average of 60 min and reduced by the start value of the time series.

The assumption of simple, linear dependencies is even stronger than for the beam walk. The simple model, with an overall \mathbb{R}^2 value of 0.97, is able to capture long-term drifts of the time series unexpectedly well [Fig. 19(a)]. Two prominent downward spikes in the Sagnac frequency are attributed to maintenance activity, thus temperature perturbation [Fig. 19(a)]. The prediction accuracy of the model for long-term drifts seems good, although the model is rather simplistic and dependencies between observables are not accounted for.

An improved, more complex model might offer efficient removal of long-term trends caused by environmental factors during post-processing. However, this does not improve short-term effects and the operational stability. The latter requires a sophisticated geometric stabilization system for all resonators. This is planned for advanced ROMY design in the near future.

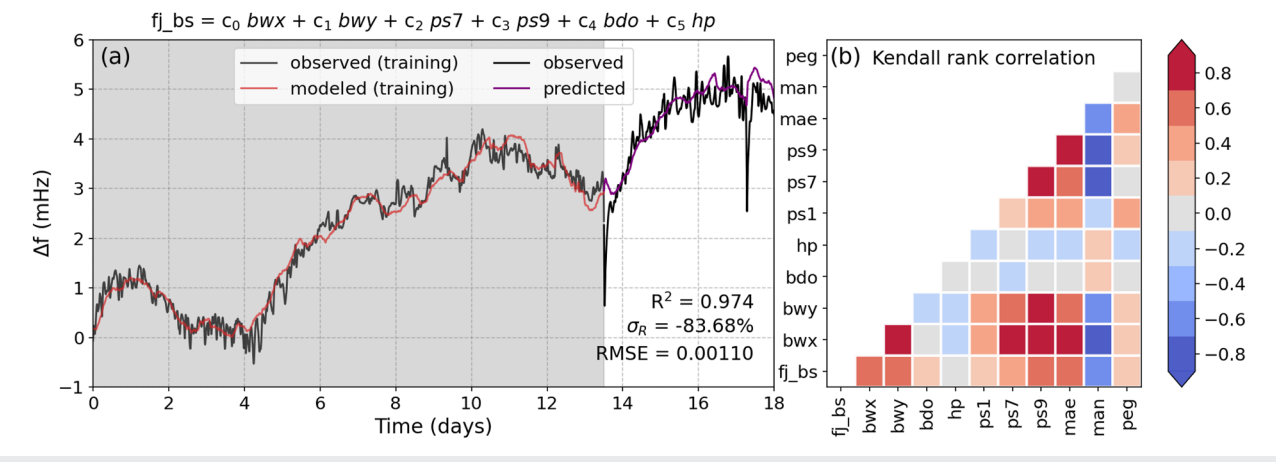


FIG. 19. (a) A time series of the smoothed Sagnac frequency at RV as observed (black) and modeled (red). Data in the gray shaded area are used to fit a linear, multivariate model as defined on top. The prediction (purple) is based on the obtained model coefficients. Kendall rank correlation coefficient matrices are shown in (b) for the smoothed Sagnac frequency without backscatter (f_b s) with other observables: bwy = beam displacement in the y-direction, bwx = beam displacement in the x-direction, peg = beam level, peg = beam litt, peg = beam litt, peg = beam displacement in the x-direction, peg = beam level, peg = beam litt, peg = beam little peg = beam litt

TABLE IV. Statistics for the linear coefficients derived using the RANSAC multivariate linear regression approach. Averages (mean and median), the standard deviation (Std), and percentiles are listed for the parameters as explained in Table III.

Parameter	Unit	Mean	Std	Median	5th %	95th %
bwx	m	0.011 472	0.000 611	0.011 474	0.010 482	0.012 407
bwy	m	0.000004	0.000000	0.000 003	0.000 003	0.000004
bdo	Pa	0.000132	0.000001	0.000 132	0.000 131	0.000 133
hp	Pa	0.000035	0.000000	0.000035	0.000034	0.000 035
ps1	°C	-0.008075	0.000 105	-0.008069	-0.008246	-0.007927
ps7	°C	0.001 355	0.000021	0.001 355	0.001 319	0.001 390
ps9	°C	-0.005954	0.000038	-0.005956	-0.006018	-0.005896
mae	rad	-23.768014	6.705 776	-23.440221	-36.212793	-13.286008
man	rad	807.019 079	3.873 066	806.709 976	801.494614	813.644735
peg	m	-0.002374	0.000 016	-0.002373	-0.002400	-0.002348

Statistical errors are obtained by estimating linear coefficients for 100 subsets, each containing a random subset of 80% of the data, using the multivariate RANSAC approach. The standard deviations and the 90% confidence interval are small for the parameters (see Table IV).

APPENDIX F: SUPPLEMENTARY FIGURES

Figure 20 provides an example of a Sagnac frequency time series for RU over several months to demonstrate drifts, shifts due to misalignment and frequency of required maintenance work.

Figure 21 provides an example of the backscatter correction applied to data of RV with residuals as signal improvement of 1–2 mHz.

Figure 22 provides an example of the backscatter correction applied to data of RZ. The correction successfully improves the signal indicated by a high variance reduction (~74%).

Figure 23 shows an example image of the laser beam taken with an IDS camera for beam tracking to illustrate the procedure. Cross sections at the beam maximum and the corresponding Gaussian fit are shown in individual panels.

Figure 24 provides an additional example of a distinct low pressure signal and its signature on the Sagnac frequency, the beam walk and the tilt record.

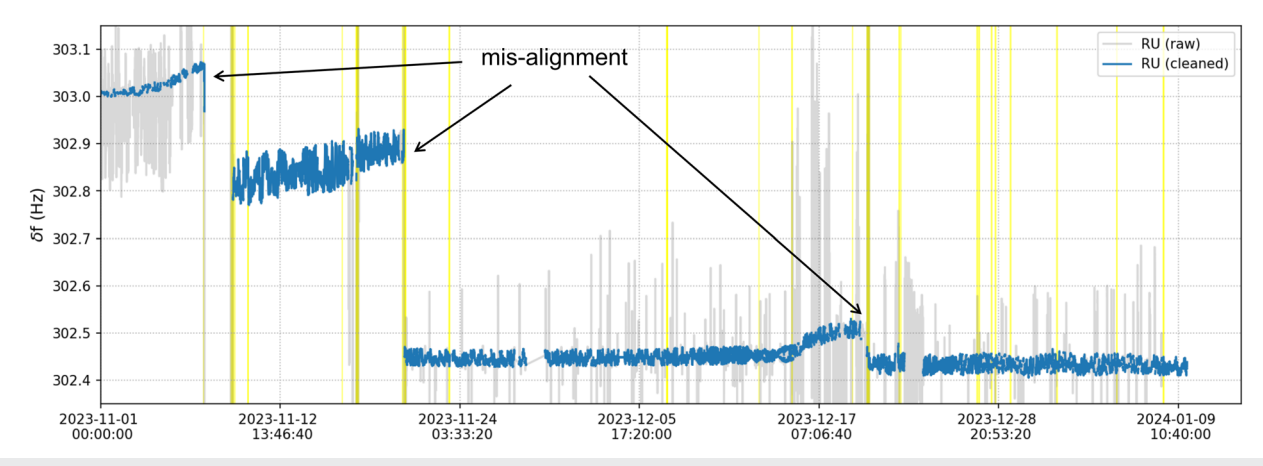


FIG. 20. Long-term Sagnac frequency time series for RU between November 01, 2023, and January 10, 2024 (gray), and without MLTI sequences (blue). Misalignments of the optical resonator that required manual re-alignment are marked. Yellow bars indicate the time periods of maintenance work.

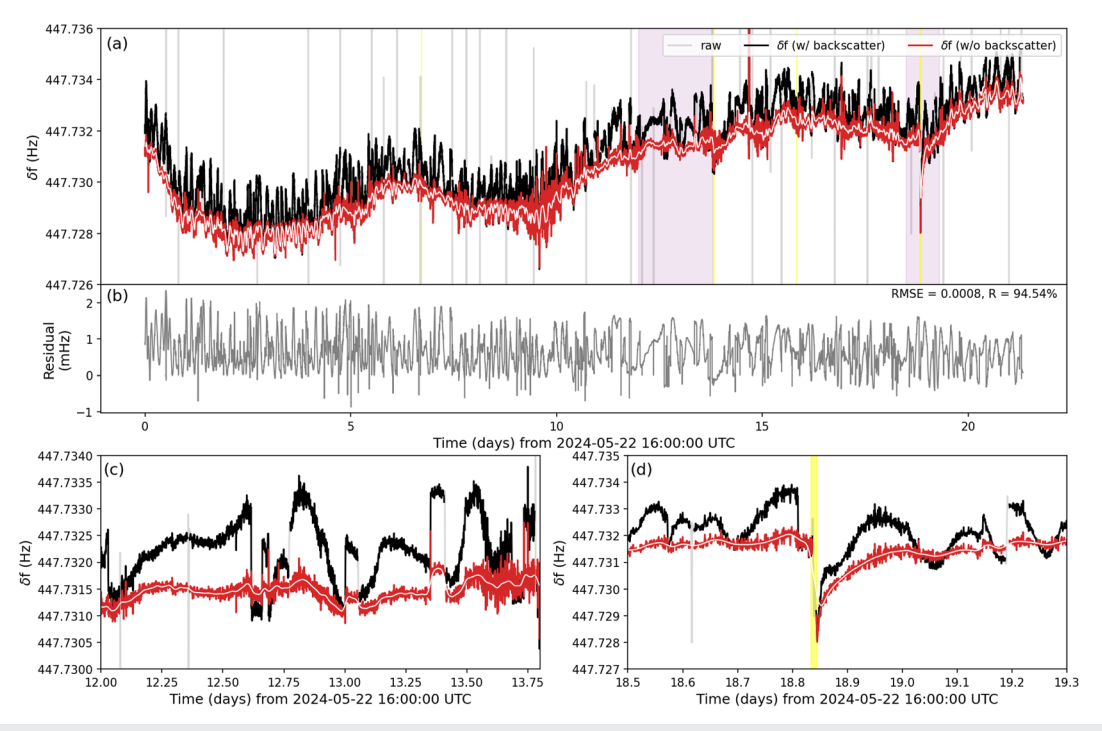


FIG. 21. (a) The time series for RV of the raw Sagnac frequency (gray) and the processed Sagnac frequency by removing MLTI launches (black) and with a backscatter correction applied (red). (b) Residual of δ f before and after backscatter correction is applied. In (c) and (d), magnified views of the data on the left and right purple shaded time intervals in (a) are shown, respectively. The yellow vertical lines indicate maintenance periods.

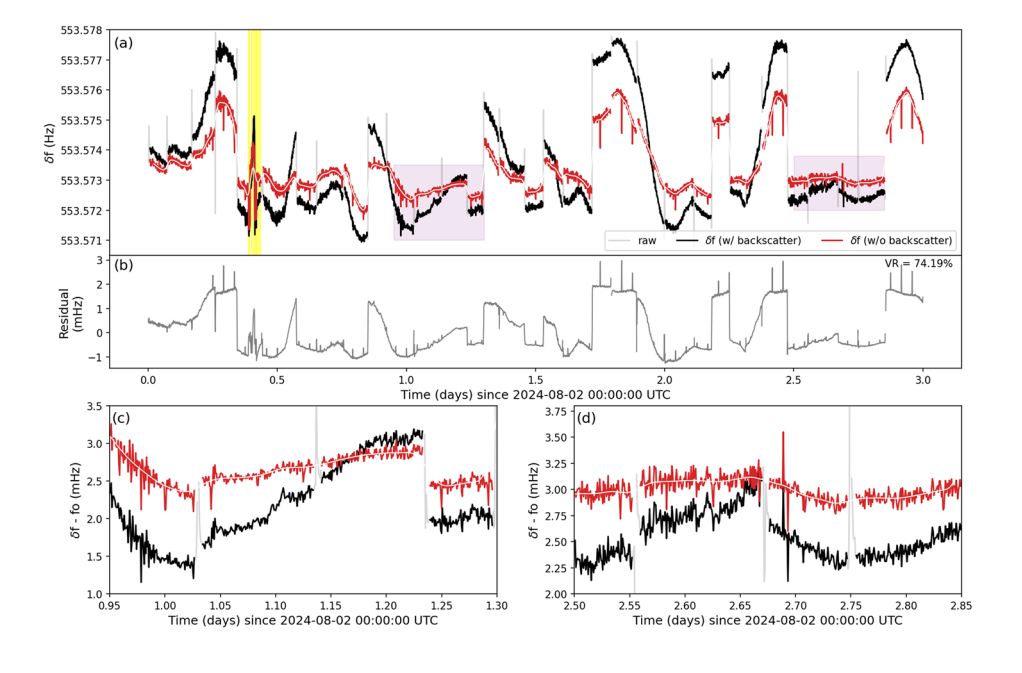


FIG. 22. (a) The time series for ROMY's horizontal ring (RZ) of the raw Sagnac frequency (gray) and the processed Sagnac frequency by removing MLTI launches (black) and with a backscatter correction applied (red). In panel (b), the difference is shown for the time series with and without backscatter contribution. (c) and (d) Magnified views of the data on the purple shaded time intervals in (a). The yellow vertical lines indicate maintenance periods.

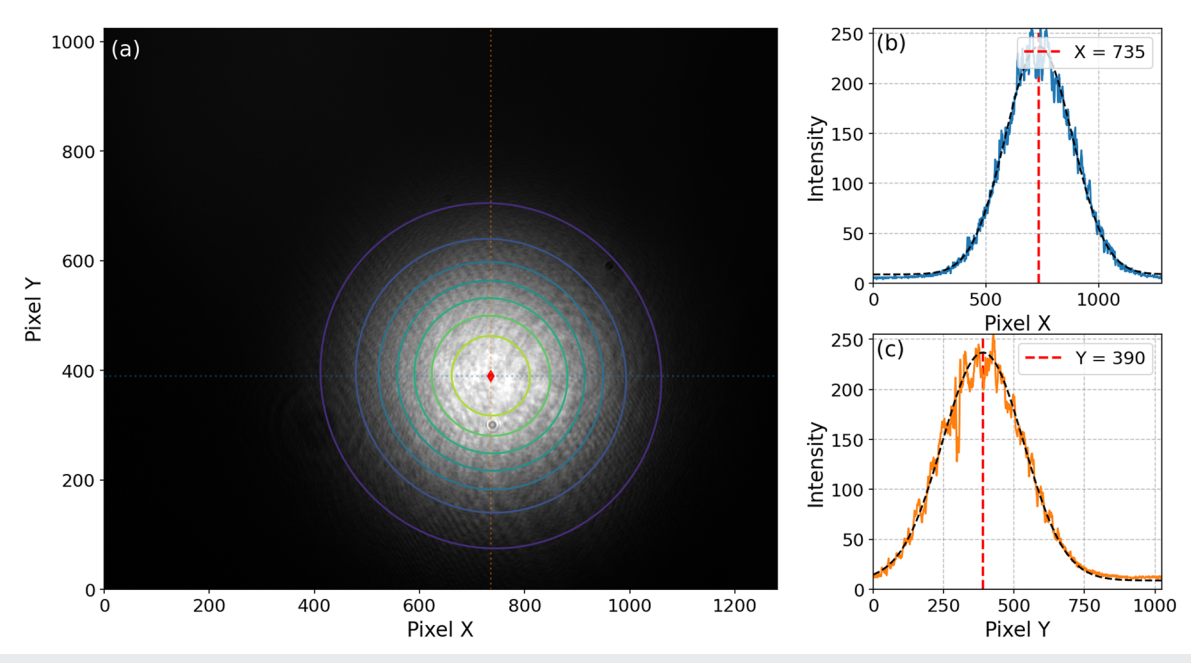


FIG. 23. (a) Example image of IDS camera for the monobeam of horizontal ring (RZ) on May 06, 2024, 22:36:04 UTC. 2D Gaussian fit is indicated as overlay with colored lines and the Gaussian peak (red diamond) at (x, y) = (554, 390). (b) and (c) Cross sections in the x- and y-directions, respectively, crossing the Gaussian peak (red dashed line). The respective 1D Gaussian fit is shown (black dashed line).

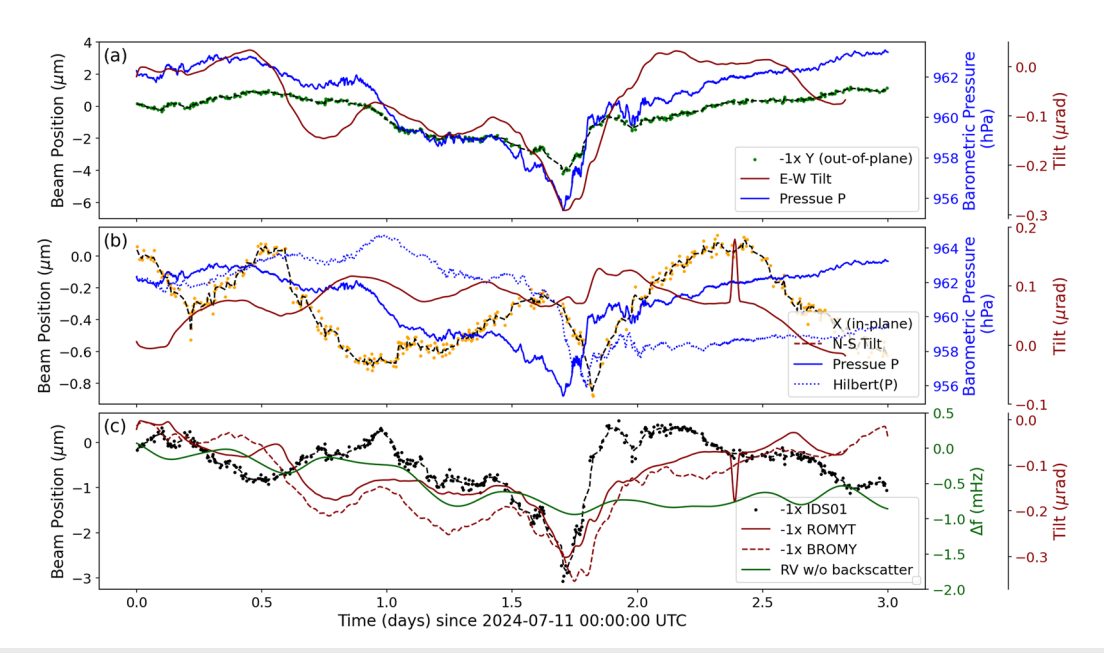


FIG. 24. Beam position of RZ is shown (a) in the reversed y-direction (=out-of-plane) and (b) in the x-direction (=in-plane) from July 11, 2024, to July 14, 2024. Outliers have been removed. The absolute barometric pressure (blue solid line) and the Hilbert transform of the barometric pressure (blue dotted line) are plotted. Tilt observations of a tiltmeter located next to the resonator corner (~50 cm distance) are shown as N-S (red dashed line) and E-W (red solid line) tilts, respectively. (c) Comparison of the absolute beam displacement $(\sqrt{X^2 + Y^2})$ of IDS01, the absolute tilt $(\sqrt{N^2 + E^2})$ for ROMYT (solid) and BROMY (dashed), as well as the 6 h moving average of the Sagnac frequency of RV without backscatter.

REFERENCES

- ¹U. Schreiber and J.-P. Wells, Rotation Sensing with Large Ring Lasers: Applications in Geophysics and Geodesy (Cambridge University Press, 2023).
- ²K. U. Schreiber, J. Kodet, U. Hugentobler, T. Klügel, and J.-P. R. Wells, Nat. Photonics 17, 1054 (2023).
- ³D. P. McLeod, G. E. Stedman, T. H. Webb, and U. Schreiber, Bulletin of the Seismological Society of America 88, 1495 (1998).
- ⁴A. Pancha, T. H. Webb, G. E. Stedman, D. P. McLeod, and K. U. Schreiber, Geophys. Res. Lett. 27, 3553 (2000).
- ⁵H. Igel, U. Schreiber, A. Flaws, B. Schuberth, A. Velikoseltsev, and A. Cochard, Geophys. Res. Lett. **32**, L08309 (2005).
- ⁶K. U. Schreiber, G. E. Stedman, H. Igel, and A. Flaws, in *Earthquake Source Asymmetry, Structural Media and Rotation Effects* (Springer, 2006), pp. 377–390.
- ⁷H. Igel, M. Bernauer, J. Wassermann, and K. U. Schreiber, in *Encyclopedia of Complexity and Systems Science*, edited by R. A. Meyers (Springer, Berlin, Heidelberg, 2014), pp. 1–26.
- ⁸M. P. Ross, K. Venkateswara, C. A. Hagedorn, J. H. Gundlach, J. S. Kissel, J. Warner, H. Radkins, T. J. Shaffer, M. W. Coughlin, and P. Bodin, Seismol. Res. Lett. **89**, 67 (2017).
- ⁹M. P. Ross, J. van Dongen, Y. Huang, H. Zhou, Y. Chowdhury, S. K. Apple, C. M. Mow-Lowry, A. L. Mitchell, N. A. Holland, B. Lantz, E. Bonilla, A. Engl, A. Pele, D. Griffith, E. Sanchez, E. A. Shaw, C. Gettings, and J. Gundlach, Rev. Sci. Instrum. 94, 094503 (2023).
- F. Bernauer, J. Wassermann, F. Guattari, A. Frenois, A. Bigueur, A. Gaillot, E. de Toldi, D. Ponceau, U. Schreiber, and H. Igel, Seismol. Res. Lett. 89, 620 (2018).
 L. R. Jaroszewicz, A. Kurzych, Z. Krajewski, J. K. Kowalski, H. A. Kowalski, and K. P. Teisseyre, Proceedings 15, 45 (2019).
- ¹²C. L. Garrido Alzar, AVS Quantum Sci. 1, 014702 (2019).
- ¹³ K. U. Schreiber, T. Klügel, A. Velikoseltsev, W. Schlüter, G. E. Stedman, and J.-P. R. Wells, Pure Appl. Geophys. **166**, 1485 (2009).
- ¹⁴K. U. Schreiber, T. Klügel, A. Velikoseltsev, W. Schlüter, G. E. Stedman, and J. P. R. Wells, Pure Appl. Geophys. **166**, 1485–1498 (2009).
- ¹⁵A. Gebauer, M. Tercjak, K. U. Schreiber, H. Igel, J. Kodet, U. Hugentobler, J. Wassermann, F. Bernauer, C.-J. Lin, S. Donner, S. Egdorf, A. Simonelli, and J.-P. R. Wells, Phys. Rev. Lett. 125, 033605 (2020).
- ¹⁶H. Igel, K. U. Schreiber, A. Gebauer, F. Bernauer, S. Egdorf, A. Simonelli, C.-J. Lin, J. Wassermann, S. Donner, C. Hadziioannou, S. Yuan, A. Brotzer, J. Kodet, T. Tanimoto, U. Hugentobler, and J.-P. R. Wells, Geophys. J. Int. 225, 684 (2021)

- ¹⁷K. Liu, F. L. Zhang, Z. Y. Li, X. H. Feng, K. Li, Z. H. Lu, K. U. Schreiber, J. Luo, and J. Zhang, Opt. Lett. **44**, 2732 (2019).
- ¹⁸R. B. Hurst, M. Mayerbacher, A. Gebauer, K. U. Schreiber, and J.-P. R. Wells, Appl. Opt. **56**, 1124 (2017).
- ¹⁹E. Maccioni, N. Beverini, G. Carelli, G. Di Somma, A. Di Virgilio, and P. Marsili, Appl. Opt. 61, 9256 (2022).
- ²⁰J. Zenner, K. U. Schreiber, and S. Stellmer, Opt. Lett. 50, 1763 (2025).
- ²¹ A. Basti, N. Beverini, F. Bosi, G. Carelli, D. Ciampini, A. D. Di Virgilio, F. Fuso, U. Giacomelli, E. Maccioni, P. Marsili *et al.*, Eur. Phys. J. Plus **136**, 537 (2021).
- ²²J. Belfi, N. Beverini, G. Carelli, A. Di Virgilio, U. Giacomelli, E. Maccioni, A. Simonelli, F. Stefani, and G. Terreni, Appl. Opt. 57, 5844 (2018).
- ²³ J. Belfi, N. Beverini, F. Bosi, G. Carelli, D. Cuccato, G. De Luca, A. Di Virgilio, A. Gebauer, E. Maccioni, A. Ortolan, A. Porzio, G. Saccorotti, A. Simonelli, and G. Terreni, Rev. Sci. Instrum. 88, 034502 (2017).
- ²⁴R. B. Hurst, G. E. Stedman, K. U. Schreiber, R. J. Thirkettle, R. D. Graham, N. Rabeendran, and J.-P. R. Wells, J. Appl. Phys. **105**, 113115 (2009).
- ²⁵B. Pritsch, K. U. Schreiber, A. Velikoseltsev, and J.-P. R. Wells, Appl. Phys. Lett. 91, 061115 (2007).
- ²⁶P. Bamforth, D. Chisholm, J. Gibbs, and T. Harrison, *Properties of Concrete for Use in Eurocode 2* (MPA The Concrete Centre, 2008).
- ²⁷E.-E. C. for Constructional Steelwork, Design of Steel Structures: Eurocode 3: Design of Steel Structures, Part 1-1: General Rules and Rules for Buildings (John Wiley & Sons, 2015).
- ²⁸ W. Zürn, J. Exß, H. Steffen, C. Kroner, T. Jahr, and M. Westerhaus, Geophys. J. Int. 171, 780 (2007).
- ²⁹ A. Brotzer, F. Bernauer, K. U. Schreiber, J. Wassermann, and H. Igel, Sensors 21, 3425 (2021).
- ³⁰ R. B. Hurst, N. Rabeendran, K. U. Schreiber, and J.-P. R. Wells, Appl. Opt. **53**, 7610 (2014).
- ³¹ A. D. Di Virgilio, N. Beverini, G. Carelli, D. Ciampini, F. Fuso, and E. Maccioni, Eur. Phys. J. C 79, 573 (2019).
- ³²D. Zou, "Ring laser gyroscopes: Using optical frequency to vary the scale factor," Ph.D. thesis (University of Canterbury, 2021).
- ³³Department of Earth and Environmental Sciences, Geophysical Observatory, University of Munich, BayernNetz (2001).
- ³⁴T. Megies, M. Beyreuther, R. Barsch, L. Krischer, and J. Wassermann, Ann. Geophys. 54, 47 (2011).